Publication Year	2015
Acceptance in OA	2020-04-22T14:43:06Z
Title	Seasonal variation of the HDO/H2O ratio in the atmosphere of Mars at the middle of northern spring and beginning of northern summer
Authors	Aoki, Shohei, Nakagawa, Hiromu, Sagawa, Hideo, GIURANNA, MARCO, SINDONI, Giuseppe, ARONICA, Alessandro, Kasaba, Yasumasa
Publisher's version (DOI)	10.1016/j.icarus.2015.06.021
Handle	http://hdl.handle.net/20.500.12386/24173
Journal	ICARUS
Volume	260

Elsevier Editorial System(tm) for Icarus
Manuscript Draft

Manuscript Number: ICARUS-13714R2

Title: Seasonal variation of the HDO/H2O ratio in the atmosphere of Mars at the middle of northern spring and beginning of northern summer

Article Type: Regular Article

Keywords: Infrared observations; Mars, atmosphere; Spectroscopy

Corresponding Author: Dr. Shohei Aoki,

Corresponding Author's Institution: Istituto di Astrofisica e Planetologia Spaziali, Istituto Nazionale di AstroFisica

First Author: Shohei Aoki

Order of Authors: Shohei Aoki; Hiromu Nakagawa ; Hideo Sagawa; Marco Giuranna; Giuseppe Sindoni ; Alessandro Aronica; Yasumasa Kasaba

Abstract: We present the seasonal variation of the HDO/H2O ratio caused by sublimation-condensation processes in a global view of the Martian water cycle. The HDO/H2O ratio was retrieved from ground-based observations using high-dispersion echelle spectroscopy of the Infrared Camera and Spectrograph (IRCS) of the Subaru telescope. Coordinated joint observations were made by the Planetary Fourier Spectrometer (PFS) onboard Mars Express (MEX). The observations were performed during the middle of northern spring (Ls = 52°) and at the beginning of summer (Ls = 96°) in Mars Year 31. The retrieved latitudinal mean HDO/H2O ratios are 4.1 ± 1.4 (Ls = 52°) and 4.4 ± 1.0 (Ls = 96°) times larger than the terrestrial Vienna Standard Mean Ocean Water (VSMOW). The HDO/H2O ratio shows a large seasonal variation at high latitudes. The HDO/H2O ratio significantly increases from 2.4 ± 0.6 wrt VSMOW at Ls = 52° to 5.5 ± 1.1 wrt VSMOW at Ls = 96° over the latitude range between 70°N and 80°N. This can be explained by preferential condensation of HDO vapor during the northern fall, winter, and spring and sublimation of the seasonal polar cap in the northern summer. In addition, we investigated the geographical distribution of the HDO/H2O ratio over low latitudes at the northern spring in the longitudinal range between 220°W and 360°W, including different local times from 10 h to 17 h. We found the HDO/H2O ratio has no significant variation (5.1 ± 1.2 wrt VSMOW) over the entire range. Our observations suggest that the HDO/H2O distribution in the northern spring and summer seasons is mainly controlled by condensation-induced fractionation between the seasonal northern polar cap and the atmosphere.

***Highlights (for review)**

This paper presents HDO/H_2O distribution on Mars at the northern spring and summer.

We performed ground-based observations using high-dispersion echelle spectroscopy.

We found seasonal increase of the HDO/H_2O ratio at the polar region (70–80°N).

The seasonal variation of HDO/H_2O ratio can be explained by phase change.

Seasonal variation of the HDO/H_2O ratio in the atmosphere of Mars at the middle of northern spring and beginning of northern summer

Shohei Aoki [a,b], Hiromu Nakagawa [b], Hideo Sagawa [c], Marco Giuranna [a], Giuseppe Sindoni [a], Alessandro Aronica [a], and Yasumasa Kasaba [b]

[b] Istituto di Astrofisica e Planetologia Spaziali (IAPS), Istituto Nazionale di Astrofisica (INAF), Via del Fosso del Cavaliere 100, 00133 Roma, Italy

[b] Department of Geophysics, Tohoku University, Sendai, Miyagi 980-8578, Japan

[c] Faculty of Science, Kyoto Sangyo University, Motoyama, Kamigamo, Kita-ku, Kyoto 603-8555, Japan

Abstract

We present the seasonal variation of the HDO/H_2O ratio caused by sublimation–condensation processes in a global view of the Martian water cycle. The HDO/H_2O ratio was retrieved from ground-based observations using high-dispersion echelle spectroscopy of the Infrared Camera and Spectrograph (IRCS) of the Subaru telescope. Coordinated joint observations were made by the Planetary Fourier Spectrometer (PFS) onboard Mars Express (MEX). The observations were performed during the middle of northern spring (*Ls* = 52°) and at the beginning of summer (*Ls* = 96°) in Mars Year 31. The retrieved latitudinal mean HDO/H_2O ratios are 4.1 ± 1.4 (*Ls* = 52°) and 4.4 ± 1.0 (*Ls* = 96°) times larger than the terrestrial Vienna Standard Mean Ocean Water (VSMOW) The HDO/H_2O ratio shows a large seasonal variation at high latitudes. The HDO/H_2O ratio significantly increases from 2.4 ± 0.6 wrt VSMOW at *Ls* = 52° to 5.5 ± 1.1 wrt VSMOW at *Ls* = 96° over the latitude range between 70°N and 80°N. This can be explained by preferential condensation of HDO vapor during the northern fall, winter, and spring and sublimation of the seasonal polar cap in the northern summer. In addition, we investigated the geographical distribution of the HDO/H_2O ratio over low latitudes at the northern spring in the longitudinal range between 220°W and 360°W, including different local times from 10 h to 17 h. We found the HDO/H_2O ratio has no significant variation (5.1 ± 1.2 wrt VSMOW) over the entire range. Our

observations suggest that the HDO/H_2O distribution in the northern spring and summer seasons is mainly controlled by condensation-induced fractionation between the seasonal northern polar cap and the atmosphere.

1. Introduction

Since the first discovery of water vapor in the Martian atmosphere using ground-based observations (Spinrad et al., 1963), the investigation of the water cycle on Mars has been one of the central topics of Martian planetary science. Space-borne observations have revealed that the global and seasonal distribution of water vapor is mainly controlled by dynamics and sublimation–condensation process between the atmosphere and the polar caps. Sublimation of water ice from the northern polar cap during spring and summer provides water vapor to the whole planet, and the water vapor re-condenses to the polar cap in fall and winter (e.g., Farmer et al., 1977; Smith, 2002; Fedorova et al., 2006; Fouchet et al., 2007; Maltagliati et al., 2008; Smith et al., 2009a). In addition to the polar latitudes, the observations have revealed the geographical distribution of water vapor at the low–middle latitudes. Two local maxima of the water vapor amount located over Tharsis (~120°W) and Arabia Terra (~330°W) were identified at middle latitudes. The maxima could be caused by atmospheric dynamics or possible release of water from the subsurface. In addition to the presence of water vapor, water ice clouds form when water vapor in the atmosphere is saturated. Thus far, two major distributions of water ice clouds have been identified (e.g., Montmessin et al., 2004). One is observed at particular low-latitude regions and is called as the "equatorial cloud belt (ECB)." This is where the air is cooled in the ascending branch of the Hadley cell during the northern spring–summer season (e.g., Smith, 2004). The other major distribution of water ice clouds occurs at middle–high latitudes and is referred to as the "polar hood clouds". These appear during the fall and spring seasons (e.g., Benson et al., 2011). In addition to the ice clouds in the atmosphere, the Gamma Ray Spectrometer (GRS) onboard Mars Odyssey discovered signals associated with subsurface water ice in the upper ~1-2 m of soil (e.g., Boyton et al., 2002; Feldman et al., 2004). Hydrogen-rich deposits (between 20 % and 100 % water-equivalent by mass) were found at high latitudes (>50°). It suggests that there are large underground water reservoirs at high latitudes. In fact, Phoenix uncovered a shallow ice table at the landing site (68.22°N) (Smith et al., 2009b). Moreover, the hydrogen-rich deposits were found not only at high latitudes, but also in low-latitude regions. The water content in low-latitude regions never drops below ~2% water-equivalent hydrogen by mass and can be as high as 8–10% around 330°W and 175°W. It implies that the subsurface water ice may present at low-latitude regions.

Water on Mars exists as vapor in the atmosphere, ice in the form of ice clouds, surface ice, and subsurface ice. The phase change between vapor and ice occurs via a sublimation–condensation process. Spatial and temporal variation of water vapor on Mars should be inseparably connected with this sublimation–condensation process. However, from the currently available observations of atmospheric H_2O on Mars, we cannot discriminate between several different physical mechanisms, e.g., atmospheric dynamics circulation, sublimation from and condensation to polar cap ice or ice clouds, and exchange with the subsurface reservoir. Mapping of the HDO/H_2O ratio allows us to infer the sublimation-condensation process. In the terrestrial case, global mapping of the HDO/H_2O ratio from a space satellite identified regions of strong evapotranspiration and condensation of water vapor (e.g., Frankenberg et al., 2009). Similar mapping of isotopic fractionation in water vapor is expected to provide deeper insight into the physical processes of the water cycle on Mars. The key theory is that the condensation process induces isotopic fractionation of water vapor due to the difference in vapor pressure. Heavier HDO vapor preferentially condensates compared to lighter H_2O vapor (e.g., Fouchet and Lellouch, 2000). Montmessin et al. (2005) calculated seasonal variations of the HDO/H_2O ratio using the General Circulation Model (GCM). They predicted that the HDO/H_2O ratio changes by a factor of 2 owing to condensation-induced fractionation in the polar region. On the other hand, no isotopic fractionation has been expected during sublimation owing very slow molecular rate of diffusion within ice. However, a recent experimental study reported that the HDO/H_2O ratio of the sublimated gas is decreased from the bulk ratio when mineral dust present in the water ice such as the Martian polar caps (Moores et al., 2012). Thus, it is still an open question whether isotopic fractionation occurs or not during sublimation of the polar caps on Mars.

HDO/H_2O ratio also has been used as a proxy to understand of the atmospheric evolution of Mars. Previous observations showed that the mean HDO/H_2O ratio in the current Martian atmosphere is 5-6 times larger than the terrestrial standard (Vienna Standard Mean Ocean Water, VSMOW; HDO/H_2O = 3.11×10^{-4}). This is probably due to atmospheric evolution, i.e., preferential escape of H atoms from the atmosphere into space for an extended period of time (e.g., Owen et al., 1988; Krasnopolsky et al., 1997; Webster et al., 2013). Understanding of the current water isotope variations in time and space can help to reveal the water history of Mars, because such variations can constrain the distribution of water reservoirs on Mars (e.g., Fisher, 2007).

So far, the distribution of the HDO/H_2O ratio has been investigated using only a few ground-based observations (e.g., Fisher et al., 2008; Novak et al., 2011). Fisher et al. (2008) showed that the HDO/H_2O ratio was not uniform but it varied within a range between 2 and 10 wrt VSMOW depending on latitude and season using the data by Mumma et al. (2003). Novak et al. (2011)

found latitudinal gradients of the HDO/H_2O ratio at Ls=50° (northern middle spring). Relatively low ratios at high latitudes were interpreted as the effect of condensation of HDO vapor over high latitudes at the middle of the northern spring. Recently, Villanueva et al. (2015) reported global maps of HDO/H_2O ratio at *Ls*=335° (northern late winter), Ls=50° (northern middle spring), and Ls=80° and 83° (northern late spring). They claimed that the averaged HDO/H_2O ratio is ~7 wrt VSMOW, which is larger than the previous observations by Owen et al. (1988) and Krasnopolsky et al. (1997). Moreover, they found correlation among HDO/H_2O ratio, atmospheric temperature, and H_2O column abundance, and possible anti-correlation between HDO/H_2O ratio and surface altitude. In addition, they found very low HDO/H_2O ratio (1-3 wrt VSMOW) at the winter hemisphere. Isotopic fractionation induced by sublimation-condensation process could explain some of the latitudinal variability, however, the phase change fractionation could not explain the reported non-uniform distribution. It might imply existence of multiple ice reservoirs having different HDO/H_2O ratios depending on their size, accessibility, and location (Fisher, 2007).

To improve our observational knowledge of this topic, we investigated the HDO/H_2O ratio during two different seasons, the northern spring (*Ls* = 52°) and summer (*Ls* = 96°), to reveal the seasonal variation. The comparison of two different seasons is expected to assist in the identification of the physical processes that cause the non-uniform distribution of HDO/H_2O. We performed ground-based observations using high-dispersion echelle spectroscopy (λ/Δλ~20,000) of the Infrared Camera and Spectrograph (IRCS) of the Subaru telescope (8.2 m) at the Mauna Kea observatory and coordinated joint observations with the Planetary Fourier Spectrometer (PFS) onboard the Mars Express (MEX).

2. Observations

2.1. Ground-based observations with Subaru/IRCS

Our ground-based observations by Subaru/IRCS were performed on January 4–5, 2012 and April 13, 2012. **Table 1** summarizes the observation conditions. The observed seasons on Mars correspond to spring (*Ls* = 52.4° and *Ls* = 52.9°) and summer (*Ls* = 96.2°) in the northern hemisphere of Mars for January 2012 and April 2012, respectively. The observational diameters of Mars were 9.3–9.4 and 11.5 arcsec on January 4–5 and on April 13, respectively. Doppler shift between Mars and Earth was -15 km/s on January 4–5 and +11 km/s on April 13. During these observations, the longitude of the sub-earth point varied from 256°W to 302°W at 23.6°N on January 4, from 237°W to 294°W at 23.6°N on January 5, and from 34°W to 60°W at 22.3°N on April 13. The longitude of the sub-solar point varied from 292°W to 339°W at 19.7°N on January

4, from 273°W to 330°W at 19.8°N on January 5, and from 344°W to 19°W at 25.0°N on April 13, 2012.

IRCS is designed to deliver diffraction-limited images at 2–5 μm, as well as to provide spectroscopy with grisms and a cross-dispersed echelle (Kobayashi et al., 2000). We used the high-dispersion echelle mode in L-band (2.85–4.16 μm) and the camera with a J-band filter (1.25 ± 0.16 μm) as a slit viewer. IRCS has a 1024 × 1024 pixel InSb array detector with a pixel size of 0.055 arcsec (slit length direction) × 0.068 arcsec (slit width direction). The longest and narrowest slit (6.69 arcsec × 0.14 arcsec) was used to maximize the spatial coverage and spectral resolving power that features an instrumental resolving power of ~20,000 with a sampling rate of ~40,000. The high spectral resolution of IRCS is essential for this study because the lines of Martian HDO and H_2O are quite narrow (line width ~0.005 cm^{-1}).

The slit was placed along the north–south direction to investigate latitudinal distribution covering the northern pole during the observations on January 5 and April 13. The slit was fixed at the sub-earth longitude that advances at a rate of about 15° in Martian longitude per hour local time (due to planetary rotation of Mars). During the observation on January 4, however, the slit was oriented along the east–west direction to investigate longitudinal distribution. For this latter case, we obtained the spectra at 15 latitudes from 0°N to 40°N by manually setting the slit on different positions.

We nodded the telescope along the slit observing Mars and sky in the A and B positions, respectively, with a difference of 30 arcsec. Subtraction of (A–B) removes the telluric emissions and other instrumental features. Flat field was obtained immediately before and after the observations. In addition, we performed standard star (*Denebola* on January 4–5 and *Regulus* on April 13) measurements at the beginning, middle, and end of each observation and Ar lamp measurements in order to investigate the instrumental line shape of IRCS.

An example of the spectrum measured by IRCS is shown in **Fig. 1**. Owing to the cross-dispersion, we could measure the following five spectral bands simultaneously: 2.94–3.01 μm (Order-19 of the IRCS grating), 3.01–3.18 μm (Order-18), 3.28–3.36 μm (Order-17), 3.49–3.57 μm (Order-16), and 3.72–3.81 μm (Order-15). The observed spectra exhibit strong absorption lines of CO_2 (627), CO_2 (628), and HDO at Order-15, CO_2 (626) at Order-16, CH_4 at Order-16 and 17, and H_2O at Order-17, 18, and 19. The wide spectral coverage of IRCS allows us to observe H_2O and HDO features simultaneously. The spatial resolution of our measurements is mainly restricted by the atmospheric seeing on the observation dates, ~0.8 arcsec on January 4–5 and ~0.5 arcsec on April 13. For the H_2O and HDO analysis, the measured spectra were binned over 10 pixels (~0.55 arcsec) along the slit to increase signal to noise ratio.

2.2. Coordinated joint observation by MEX/PFS

PFS is a double-pendulum interferometer mainly designed for atmospheric analyses, such as measuring the 3-D temperature field in the lower atmosphere, the variations of minor constituents, and the optical properties of aerosols (Formisano et al., 2005). It has two spectral channels, one is the Short Wavelength Channel (SWC) and the other is the Long Wavelength Channel (LWC). The SWC covers the spectral range between 1750 and 8200 cm^{-1} and the LWC covers the spectral range between 250 and 1700 cm^{-1}, both with a sampling step of 1.0 cm^{-1}. The spectral resolution is 1.3 cm^{-1} without apodization and 2 cm^{-1} when a Hamming function is applied to the interferograms. One of the advantages of PFS is its wide spectral coverage combined with relatively high spectral resolution.

We planned and performed coordinated joint measurements by MEX/PFS from April 10 to 16 (within ±3 days from the Subaru/IRCS observation). The original purpose of this joint observation was to compare H_2O retrievals between IRCS and PFS. However, the abundances of H_2O could not be retrieved from the IRCS data because of the high terrestrial humidity during the joint observation. Therefore, the PFS measurements were used to retrieve H_2O abundances and were subsequently coupled with the HDO data from Subaru/IRCS to derive the HDO/H_2O ratio (there was no problem retrieving both H_2O and HDO from Subaru/IRCS data for the other observations carried out in January 2012). During the planned period (April 10 to 16) of the coordinated observations, PFS observations were performed in 26 orbits across Mars (MEX orbit #10541–10567). Unfortunately, PFS had some problems with the motion of the double-pendulum during this period of simultaneous observation with the Subaru/IRCS. However, PFS worked nominally in the 4 orbits listed in **Table 2** and these observations have been successfully included in this work (as quasi simultaneous observations).

3. Method of analysis

3.1. Retrieval of H_2O and HDO abundances from Subaru/IRCS data

We retrieved H_2O abundances from the absorption lines at 3035.78356 cm^{-1} (3.29 μm, Order-17) and 3216.52218 cm^{-1} (3.10 μm, Order-18) and HDO abundances from the lines at 2672.59294 cm^{-1} and 2677.71967 cm^{-1} (both around 3.74 μm, Order-19). We performed retrievals for each line independently in order to evaluate the accuracy of our retrievals. **Table 3** describes the line parameters obtained from the HITRAN 2008 database (Rothman et al., 2009). As shown in **Fig. 1**, there are multiple H_2O and HDO lines in the measured spectral range. However, most of the H_2O

lines are saturated or not strong enough, and CO_2 isotopic lines under the finite spectral resolution of IRCS contaminate most of the HDO lines on the measured spectra. We carefully selected the absorption lines to be used in this work. The selected lines satisfy the following conditions: strong enough (i.e., line strength is order of 10^{-22} for H_2O and 10^{-24} for HDO), not saturated, minimal instrumental effect (i.e., line center is stable within ~1 pixel along the slit), and minimal contamination from the other lines (i.e., the other terrestrial [O_3, N_2O, CH_4, and H_2O isotopes], Martian CO_2, and solar lines).

Since the Martian H_2O and HDO lines appear on the wings of the deep terrestrial ones (the Martian lines are shifted ~2 pixels from the terrestrial lines due to the Doppler shift), the contribution from the terrestrial atmosphere should be separated in order to extract the Martian lines. The extraction requires special considerations of the narrowness of the Martian lines (~1/10 of the IRCS spectral resolution) and of the intrinsic (anamorphic) optical properties of IRCS that lead to an irregular mapping of the spatial and spectral dimensions on to the detector array. For removal of telluric absorptions, co-measured spectra of nearby reference stars are often used in ground-based observations. However, extrapolating the reference star (point-source) signal to an extended object introduces systematic errors. In addition, since the method with standard stars requires atmospheric stability and the same observed air mass between the target and reference stars, it does not always guarantee the quality of the calibration. To solve these problems, we numerically synthesized the terrestrial atmospheric opacity by developing a dedicated line-by-line radiative transfer model and fitted it to the measurement spectra to obtain the telluric absorptions during our observations.

Our model is based on clear-sky atmosphere model and takes into account the atmospheric opacities due to terrestrial lines of H_2O, HDO, and O_3, Martian lines of H_2O, HDO, and CO_2 isotopologues (626, 627, 638), solar lines, and the instrumental line shape of IRCS. The line parameters were obtained from the HITRAN 2008 spectroscopic database (Rothman et al., 2009). Isotopic ratios of CO_2 (627) and CO_2 (638) were obtained from recent results by Curiosity/TLS (Webster et al., 2013; reported isotopic ratios of CO_2 (627) and CO_2 (638) are 7.618×10^{-4} and 4.928×10^{-5}, respectively). The expected signal intensity $I(x_0)$ at pixel-point x_0 was calculated as follows:

$$I(x_0) = [(ax+b) \times t_{solar}(x) \times \exp(-\tau_E(x) - \tau_M(x))] \otimes ILS(x_0 - x, w_{ILS}),$$

where x is pixel-point with a sampling rate of ten milli-pixels (x_0 and x are a function of wavelength), a and b are the scaling factors for continuum, t_{solar} is the transmittance of the solar lines, τ_E is the total optical depth of the terrestrial lines, τ_M is the total optical depth of the Martian lines, and ILS is the instrumental line shape of IRCS. The transmittance of the solar spectrum was obtained from the database of the high-spectral-resolution observation performed by the ACE/FTS

(Hase et al., 2010). The instrumental line shape of IRCS was retrieved from Ar lamp measurements. Since this analysis is sensitive to the line shape and especially to its wing, accurate characterization of the ILS is indispensable to retrieve the Martian H_2O and HDO abundances correctly. We found that the instrumental line shape can be expressed as a function of one parameter (its width W_{ILS}) depending on pixel position over the detector, and this function can be defined by a combination of two Gaussian functions (see *Appendix A* in detail). For calculations of the terrestrial lines, we considered 32 atmospheric layers from 4 km to 50 km. The vertical profiles of temperature, pressure, water vapor, and O_3 in the terrestrial atmosphere were obtained from US standard atmosphere. Since the line shapes of the terrestrial atmosphere are dominated by molecular collisions, we considered the collisional line width at each atmospheric layer and summed the optical depths along the 32 atmospheric layers:

$$\tau_E(x) = \sum_j \frac{\eta N_j S(T_j)\alpha_L(T_j,P_j)/dw}{\pi[(x-x_0)^2+(\alpha_L(T_j,P_j)/dw)^2]} \times z_j,$$

where $\tau_E(x)$ is the total optical depth at x pixel-point, η is the telluric air mass, N_j is the column abundance of the gas at the j-th layer, T_j is the temperature at the i-th atmospheric layer, $S(T_j)$ is the line strength at T_j K, α_L is the collisional line width, dw is the dispersion of the IRCS echelle mode in L-band (0.763 □/pixel at order18, 0.809 □/pixel at order-17, and 0.914 □/pixel at order-15), x_0 is the central pixel-point of the terrestrial line, and z_j is the thickness of the layer. The temperature correction of the line intensity is referred to Rothman et al. (1998) by using the total internal partition sum from Gamache et al. (2000).

Line width of H_2O and HDO in the Martian atmosphere is dominated by the Doppler line width (e.g., Krasnopolsky et al., 2004), because the pressure in the atmosphere is relatively low. Therefore, we computed the optical depth considering the Doppler line widths:

$$\tau_M(x) = \sum_j \frac{\mu N_j S(T_j)}{\sqrt{\pi}\alpha_D(T_j)/dw} \exp(-[\frac{(x - x_0 + ds/dw)}{\alpha_D(T_j)/dw}]^2) \times z_j,$$

where $\tau_M(x)$ is the total optical depth at x pixel-point, μ is the total air mass on Mars, α_D is the Doppler line width, and ds is Doppler shift. For the Martian atmosphere, we considered 10 atmospheric layers from 0 km to 20 km, and the vertical profiles of temperature, pressure, and water vapor were derived from Mars Climate Database ver 4.3 (http://www-mars.lmd.jussieu.fr/mars/access.html). We assumed the effects of dust and ice aerosols to be negligible at this wavelength; accordingly, these were not included in the radiative transfer calculation.

The measured signals include both solar radiation reflected at the Martian surface (2-way path in the Martian atmosphere: Sun–Mars–Earth) and the thermal radiation of the Martian surface (1-way path: Mars–Earth). Thus, the total air mass μ is given by

$$\mu = r_s(\mu_s + \mu_e) + (1 - r_s)\mu_e,$$

where r_s is the rate of solar radiation, $(1–r_s)$ represents the rate of the thermal radiation, μ_s is the Sun-to-surface air mass, and μ_e is the surface-earth air mass. Our radiative transfer model showed that the contribution of thermal radiation from the Martian surface is negligible (i.e., $r_s = 1.0$) at the H_2O spectral range. Conversely, at the HDO spectral range, the contribution of thermal radiation must be taken into account. The rate r_s was retrieved using a strong solar line at 2669.7849 cm^{-1} by comparing the observed spectrum with the synthetic spectrum of the solar line. **Fig. 2** shows the retrieved rate of surface radiation $(1-r_s)$ retrieved from the IRCS data. The rates are variable depending on surface albedo and temperature. The enhancement of surface radiation rate $(1-r_s)$ at 280-320°W and 0-20°N appeared in the January data can be explained by low surface albedo (Christensen et al., 2001), and the latitudinal gradient appeared in the April data can be explained by decrease of surface temperature toward polar region. The relatively high rate at high-latitude region (>70°N) found in January data is probably caused by high surface albedo due to the presence of the seasonal polar cap on the ground.

For retrieval, the synthetic spectra were calculated in the limited spectral range of ±7 pixels (~ ±0.5 cm^{-1}) from the line center for each H_2O line, and ±5 pixels (~ ±0.3 cm^{-1}) from the line center for each HDO line. We retrieved the following five parameters: scaling factor for the continuum (*a* and *b*), center pixel-point of the deep terrestrial line x_0, width of instrumental line shape w_{ILS}, total column density of the terrestrial water vapor, and total column density of the Martian water vapor. We set the spectral resolution as an unknown parameter because it varies along the slit and dispersion direction. The total column density of the terrestrial water vapor was assumed as a constant value along the slit. The retrieval was performed by setting a parameter domain for the column density of Martian water vapor from 0 pr-μm to 25 pr-μm with intervals of 1 pr-μm for H_2O and 0 pr-nm to 100 pr-nm with intervals of 1 pr-nm for HDO. Then, for each condition of Martian H_2O and HDO abundances, we retrieved the other 5 parameters using Levenberg–Marquardt non-linear minimization algorithm. Finally, we derived the Martian H_2O and HDO column densities that provide the minimum values for chi-squares. To check our retrieval scheme, we applied the retrieval algorithm to standard star data as well as Mars observations. **Figures 3** and **4** show examples of the fitting analysis in the H_2O and HDO spectral ranges, respectively. No residual signal is present from the standard star observation, as expected. This indicates that the signal derived from Mars data represents the real Martian contribution.

There are two sources of error in the retrieved Martian H_2O and HDO abundances: instrumental noise and uncertainty in the forward (radiative transfer and IRCS instrumental) model. The instrumental noise was estimated from standard deviation (1-sigma) of the residuals between IRCS data and best-fit synthetic spectrum. Regarding the forward model error, the dominant factor is uncertainty in the temperature profile obtained from the Mars Climate Database, whose uncertainty is expected to be ~5% (Sindoni et al., 2011). This uncertainty propagates to the errors of ~7% and ~1% in the retrieved H_2O abundances from 3035 cm^{-1} and 3216 cm^{-1} and ~5% and ~4% in the retrieved HDO abundances, respectively. Finally, the uncertainties in the retrieved H_2O or HDO abundances σ were given by

$$\sigma = \sqrt{\sigma_n{}^2 + \sigma_m{}^2},$$

where σ_n is error due to instrumental noise, and σ_m represents error due to the model. After the errors were evaluated, the H_2O abundances retrieved from the absorption lines at 3035 cm^{-1} and 3216 cm^{-1} and the HDO abundances from the lines at 2672 cm^{-1} and 2677 cm^{-1} were compared, respectively. We excluded results of the two retrieved values (H_2O or HDO abundances) that were inconsistent beyond 2σ as "low confidence" results. Note that the inconsistent results were less than 15% of the whole data set. Lastly, the derived H_2O abundances, HDO abundances, and their errors were calculated from the weighted averages:

$$y = \frac{w_a y_a + w_b y_b}{w_a + w_b},$$
$$\sigma = \frac{1}{\sqrt{w_a + w_b}},$$

where y represents the derived H_2O or HDO abundance, y_a and y_b are the values retrieved from each of the lines, and w_a and w_b are given by

$$w_a = \frac{1}{{\sigma_a}^2},$$
$$w_b = \frac{1}{{\sigma_b}^2},$$

where σ_a and σ_b are the errors retrieved from each of the lines.

3.2. Retrieval of H_2O abundances from MEX/PFS data

We retrieved H_2O abundances from PFS observations listed in **Table 2**. For the H_2O retrievals, the absorption band from 3780 to 3950 cm^{-1} at the Short Wavelength Channel (SWC) was used (Tschimmel et al., 2008; Sindoni et al., 2011). We averaged 9 consecutive spectra with a sampling rate of every two spectra in order to improve the SNR and the accuracy of the retrieved H_2O abundances. **Figure 5** shows an example of averaged PFS spectrum in the considered spectral range, and the best-fit synthetic spectrum. We retrieved H_2O abundances using a fast radiative transfer model developed for PFS data processing (Ignatiev et al., 2005) and least-squares method. The details of the retrieval algorithm can be found in Sindoni et al. (2011). The uncertainty in the retrieved H_2O mixing ratio is about 19% total (Sindoni et al., 2011).

4. Latitudinal distribution at *Ls* = 52° (northern spring)

Figure 6 shows latitudinal distribution of column-integrated H_2O and HDO abundances retrieved from Subaru/IRCS observations carried on January 5, 2012 (*Ls* = 52°) and the H_2O abundances taken from Mars Climate Database (MCD) ver-5.0 (http://www-mars.lmd.jussieu.fr/mars/access.html) for comparison. Different colors indicate the observed longitudes. These values have been normalized by surface pressure in order to remove the effect of topography. The retrieved H_2O abundances range from 4 pr-μm to 15 pr-μm (1 pr-μm = 3.34×10^{18} cm^{-2}), and exhibit maximum values around 60–70°N. On the other hand, the H_2O abundances predicted by MCD range from 5 pr-μm to 15 pr-μm, and show a maximum value around 60°N. Our observed H_2O abundances show general agreement with those from the MCD in terms of absolute values and latitudinal distribution. In addition, the longitudinal trend at the edge of Arabia Terra (over 302°W and 298°W at middle latitudes) appears both in the observation and model.

In the northern spring season (*Ls* = 52°), the edge of the northern polar cap is expected to be around 70°N, according to the observations by near-infrared spectroscopy (e.g., Appéré et al., 2011). Since surface temperature exceeds water condensation temperature at the edge of the polar cap, sublimation of the water ice cap would occur there. Indeed, the previous observations of water vapor during this season exhibit its enhancement at the edge of polar cap (e.g., Fouchet et al., 2007; Pankine et al., 2010). Thus, the enhancement of H_2O shown in our observations is likely due to sublimation of water ice.

The latitudinal distribution of HDO appears slightly different to that of H_2O. The retrieved HDO abundances range from 3 pr-nm to 17 pr-nm (1 pr-nm = 3.34×10^{15} cm^{-2}) and have a maximum value around 30–40°N. The difference between H_2O and HDO produces latitudinal gradients in the HDO/H_2O ratio. **Fig. 7** shows the latitudinal distribution of the HDO/H_2O ratio retrieved from the Subaru/IRCS observation (left panel), their mean values averaged over the faced longitude (256–302°W), and values predicted by the GCM model of Montmessin et al. (2005) (right panel). The derived mean HDO/H_2O ratio ranges between 5.0 ± 0.9 wrt VSMOW (at 30°N) and 2.4 ± 0.6 wrt VSMOW (at 80°N). The global mean value of the HDO/H_2O ratio and its standard deviation are 4.1 ± 1.4 wrt VSMOW. The distribution exhibits a maximum around sub-solar latitudes (20–40°N) and decreases at high latitudes (>60°N). As shown in **Fig. 7**, such a latitudinal gradient was also predicted by the GCM model based on condensation-induced fractionation (Montmessin et al., 2005). The model predicted that the HDO/H_2O ratio would decrease from 5 wrt VSMOW to 2 wrt VSMOW owing to preferential condensation of HDO vapor at high latitudes. We consider this depletion of HDO around 50–80°N is mainly due to the condensation of water vapor on the polar cap. In fact, the previous observation of surface composition detected the formation of a water ice cap over the polar cap at 70–90°N (e.g., Appéré et al., 2011) and the GCM suggested the formation of polar hood clouds at 50–90°N (Montmessin et al., 2004).

5. Latitudinal distribution at *Ls* = 96° (northern summer)

We retrieved the latitudinal distribution of the HDO/H_2O ratio during the northern summer (*Ls* = 96°) using HDO abundance obtained by Subaru/IRCS data and H_2O abundances retrieved from MEX/PFS data in order to investigate seasonal variation. HDO could not be detected from IRCS data with enough accuracy below 40°N owing to the high terrestrial humidity during the ground-based observation. **Fig. 8** shows the latitudinal distribution of the H_2O column density retrieved from PFS/SWC data (left panel) and the HDO column density retrieved from Subaru/IRCS data (right panel). These values have been normalized by surface pressure to remove the effect of topography. We found that both H_2O and HDO column densities have a large value in the polar region during the northern summer (*Ls* = 96°).

In order to derive the HDO/H_2O ratio from these data, we calculated the mean profile of H_2O column density retrieved by PFS with the latitudinal grid of the SUBARU observation. For that, the H_2O column densities within the latitudinal footprint of SUBARU observation (i.e., atmospheric seeing during the observation) were averaged. The red curve in the left panel of **Fig. 8** shows the mean profile of H_2O column density. The black points shown in **Fig. 9** represent the

HDO/H_2O ratio calculated by the profiles, and the red curve shown in **Fig. 9** is the averaged HDO/H_2O ratio in order to compare with that of *Ls*=52° (the blue curve shown in **Fig. 9**). The mean value (averaged over all observed longitudes and latitudes) of the HDO/H_2O ratio at *Ls* = 96° and its standard deviation are 4.4 ± 1.0 wrt VSMOW. Although the error values are relatively large (mainly owing to the standard deviation of the H_2O column density from PFS data and longitudinal variability), the latitudinal distribution of HDO/H_2O ratio at *Ls*=96° is more uniform profile than the one observed at *Ls*=52°. An interesting result from **Fig. 9** is the seasonal variation of HDO/H_2O ratio over the latitude range between 70°N and 80°N. We found that the HDO/H_2O ratio increased from 2.4 ± 0.6 wrt VSMOW (*Ls* = 52°) to 5.5 ± 1.1 wrt VSMOW (*Ls* = 96°) at the high latitude. As described in Section 4, the relatively low value of the HDO/H_2O ratio at *Ls* = 52° can be explained by condensation of water vapor. Since the water vapor abundances in the polar region exhibit a drastic increase from *Ls* = 52° to *Ls* = 96°, the seasonal increase of the HDO/H_2O ratio from *Ls* = 52° to *Ls* = 96° can be considered to be due to sublimation of the polar water ice cap. Moreover, this relatively uniform latitudinal distribution of HDO/H_2O ratio *Ls* = 96° implies that the isotopic fractionation during sublimation is small and is beyond the sensitivity of this analysis. The observed seasonal variation suggests that the sublimation–condensation process can induce a change in the isotopic fractionation by a factor of 2.

Note that the IRCS and PFS measurements were taken at different local times on Mars (IRCS: 9-10h, PFS: 16h). This may cause systematic error in the retrieved HDO/H_2O ratio. However, Phoenix measurements showed no significant difference in H_2O abundance between 9h and 16h (Smith et al., 2009b). Moreover, recent remote-sensing studies by MEX/SPICAM and MGS/TES show that local time variation of total H_2O column is small at this season (e.g., Pankine and Tamppari, 2015; Trokhimovskiy et al., 2015). The systematic error in the HDO/H_2O ratio can be estimated to be less than ~10%. Therefore, we assume that the systematic error in the HDO/H_2O ratio due to using the different local time observations by IRCS and PFS can be less than ~10%. The seasonal increase of HDO/H_2O ratio over the latitude range between 70°N and 80°N is still significant even if the systematic error is taken into account.

6. Geographical distribution over low latitudes at *Ls* = 52° (northern spring)

We investigated the geographical distribution of the HDO/H_2O ratio over low latitudes at the northern spring (*Ls* = 52°) in the longitudinal range between 220°W and 360°W, including various local times from 10 h to 17 h. **Fig. 10** shows the longitudinal distribution of column-integrated H_2O and HDO abundances retrieved from the Subaru/IRCS observations carried out on January 4, 2012. These values have been normalized by surface pressure in order to remove the effect of topography. The retrieved H_2O abundances are distributed in the range from 4 pr-μm to 18 pr-μm, and the HDO abundances range from 5 pr-nm to 19 pr-nm. The retrieved H_2O abundances are consistent with the typical abundance during this season reported by the space-borne observations. For example, MGS/TES and Viking/MAWD results determined that the longitudinal mean abundances at this season are between 10 pr-μm and 15 pr-μm (e.g., Smith, 2002). The retrieved longitudinal distribution of water vapor exhibits a local maximum over Arabia Terra (~330°W), according to both H_2O and HDO abundances. **Fig. 11** illustrates the longitudinal distribution of the HDO/H_2O ratio retrieved from the Subaru/IRCS observations (top panel) and the value averaged over all latitudes (bottom panel). The global mean value of the derived HDO/H_2O ratio and its standard deviation are 5.1 ± 1.2 wrt VSMOW. The local enhancement of water vapor abundances over Arabia Terra has been depicted in a seasonal-averaged map of water vapor using spacecraft-borne measurements with MGS/TES (Smith, 2002) and MEX/PFS (Fouchet et al., 2007; Tschimmel et al., 2008; Sindoni et al., 2011). On the other hand, as shown in **Fig. 11**, there is no significant longitudinal variation in the HDO/H_2O ratio. Although the results cannot constrain the sources of local enhancement, i.e., atmospheric dynamics or sublimation from subsurface ice, we have demonstrated that there is no significant longitudinal distribution over Arabia Terra.

These observations also covered different local times ranging from 10 h to 17 h, although not for the same longitudes. **Fig. 12** shows the local time distribution of H_2O and HDO abundances normalized by surface pressure. The retrieved water vapor exhibits a local maximum around 12–13 h that corresponds to Arabia Terra (~330° W). **Fig. 13** represents the local time dependence of the HDO/H_2O ratio retrieved from the Subaru/IRCS observation. It shows that the distribution of HDO/H_2O is no significant variation (5.1 ± 1.2 with respect to VSMOW) in the local time range between 10 h and 17 h. Note that recent observations reveal a significant depletion of HDO at dawn that may be explained by condensation-induced fractionation due to cloud formation (Villanueva et al., 2008; Villanueva et al., 2013; Novak et al., 2014). Further observation is needed to address this issue, because the dawn side was not covered by our observations.

7. Comparison with the previous observations

The latitudinal mean HDO/H_2O ratios retrieved from our observations are 4.1 ± 1.4 (Ls = 52°) and 4.4 ± 1.0 (Ls = 96°) wrt VSMOW, which agrees with the global mean values reported by previous ground-based observations by Owen et al. (1988) [6 ± 3 wrt VSMOW] and Krasnopolsky et al. (1997) [5.5 ± 2.0 wrt VSMOW] but smaller than the value reported by Villanueva et al. (2015) [~ 7 wrt VSMOW]. One possible explanation for this discrepancy is temporal variation of the HDO/H_2O ratio (seasonal, localtime, or inter-annual variation). The other possible explanation is due to systematic error in the analysis. For instance, in this analysis, the effect of dust and water ice was not taken into account. This may give an impact the retrieved HDO abundance (see SOM of Villanueva et al., 2015). The implementation of the aerosol effect in our retrieval is one of the future works.

As shown in **Fig. 7**, we found that the retrieved latitudinal distribution at *Ls* = 52° exhibits a maximum around sub-solar latitudes (20–40°N) and decreases at high latitudes (>60°N), which was also found by Novak et al. (2011). The observation by Novak et al. (2011) was performed in the same season (*Ls*=50°) as our observation but for a different Martian year (MY 29), longitude (153°W), and local time (9:40) by the IRTF/CSHELL. The HDO/H_2O ratio retrieved by Novak et al. (2011) peaks at 6.9 ± 0.2 wrt VSMOW in the sub-solar region and decreases to 3.8 ± 0.3 towards the pole. Although our values are smaller than those obtained by Novak et al. (2011), the two observations have a similar distribution that peaks near the sub-solar latitude and decreases toward the pole. Moreover, Villanueva et al. (2015) reported the map of HDO/H_2O ratio taken by the IRTF/CSHELL in the same season (*Ls*=50°), the same Martian year (MY 29), and including same longitude (153°W) of the observation by Novak et al. (2011). However, the map by Villanueva et al. (2015) does not show the depletion of HDO at the high latitudes region. Villanueva et al. (2015) also revealed correlation between HDO/H_2O ratio and H_2O column abundance. The positive correlation is agreed with the concept of the Rayleigh distillation considered in the GCM model (Montmessin et al., 2005). On the other hand, Fisher et al. (2008) reported that the HDO/H_2O ratio is very large when the atmosphere's water vapor column is small from the data by Mumma et al. (2003). The anti-correlation between H_2O column density and HDO/H_2O ratio was interpreted as the possible effect of existence of multiple ice reservoirs having different HDO/H_2O ratios depending on their size, accessibility, and location. **Fig. 14** shows the relationship between H_2O column density and HDO/H_2O ratio from our results. Our result at *Ls*=52° also suggests the anti-correlation. Further observations are necessary to constrain these issues. Furthermore, Villanueva et al. (2015) reported possible anti-correlation between HDO/H_2O ratio and surface altitude. Although possible regionalism could be seen in our results, we cannot make sure if it is real variation since the error values are large. Regionalism of HDO/H_2O is beyond the scope of this paper.

As shown in **Fig. 11**, we found that the HDO/H_2O ratio was no significant variation (5.1 ± 1.2 wrt VSMOW) in the longitudinal range between 220°W and 360°W at *Ls*=52.4°. Novak et al. (2014, conference proceeding) reported the longitudinal distribution of HDO/H_2O ratio over the same area but at different season (*Ls*=72.5°). The HDO/H_2O ratio at Ls=72.5° reported by Novak et al. (2014) is distributed between 2 to 5 wrt VSMOW (see the **Fig. 3B** of Novak et al. (2014)). The

HDO/H_2O values are lower than those of our results at *Ls*=52.4°. Although the reason is not clear at the moment, the seasonal variation of HDO/H_2O ratio at low latitudes could be related with the fact that Villanueva et al. (2015) found very low HDO/H_2O ratio (1-3 wrt VSMOW) at the winter hemisphere. Similar seasonal decrease of the HDO/H_2O ratio at the low-latitude region also can be seen in the maps (at *Ls*=50° and 80°) reported by Villanueva et al. (2015).

8. Summary

In this study, seasonal variation of HDO/H_2O distributions by latitude during the northern spring (*Ls* = 52°) and summer (*Ls* = 96°) was investigated. The derived seasonal variation of the HDO/H_2O ratio and global view of the water cycle on Mars inferred from our observations is summarized in **Fig. 15**. We found seasonal increase of the HDO/H_2O ratio at the polar region (70–80°N), from 2.4 ± 0.6 wrt VSMOW (*Ls* = 52°) to 5.1 ± 0.7 wrt VSMOW (*Ls* = 96°). The seasonal increase can be explained by the interaction between the atmosphere and the north polar cap: condensation of water vapor occurs as polar hood clouds and/or the seasonal polar cap form in the northern spring (*Ls* = 52°), and sublimation of the polar water ice cap occurs in the northern summer (*Ls* = 96°). On the other hand, the latitudinal mean HDO/H_2O ratios do not show a significant seasonal variation, with values of 4.1 ± 1.4 (*Ls* = 52°) and 4.6 ± 0.7 (*Ls* = 96°). We found the HDO/H_2O ratio has no significant variation (5.1 ± 1.2 wrt VSMOW) over low latitudes during the northern spring in the longitudinal range between 220°W and 360°W for different local times from 10 h to 17 h. As shown in **Fig. 15**, we did not take into account the effects of subsurface-atmosphere interaction in the interpretation of the results since it is still unknown that how much the ground ice interacts with atmospheric water vapor and how much they induce isotopic fractionations. However, our results suggest that HDO/H_2O distribution in the atmosphere is mainly controlled by condensation-induced fractionation between the northern polar cap and the atmosphere.

Still, further observations are necessary to conduct open issues. For example, relationship between H_2O column density and HDO/H_2O ratio and its interpretation are not fully understood. Very low HDO/H_2O ratio (1-3 wrt VSMOW) at the winter hemisphere reported by Villanueva et al. (2015) might be related to subsurface-atmosphere interaction. In order to increase data set, we plan to investigate the HDO/H_2O ratio by comparing between the HDO map observed by IRTF/TEXES (e.g., Encrenaz et al., 2010) and the H_2O map retrieved from MEX/PFS. In addition, Nadir and Occulation for Mars Discovery (NOMAD) onboard ExoMars Trace Gas Orbiter (Vandaele et al., 2011) will perform to measure maps of HDO/H_2O ratio and its vertical profile are obtained from the Mars Orbiter. It will allow us to obtain a complete picture of its geographical and seasonal distributions.

Acknowledgements

This work was supported by a Grant-in-Aid for JSPS Fellows (#233113). This work was also supported by a grant-in-aid for Scientific Research (22340142, 24403007, and 15H05209) from the Japan Society for the Promotion of Science, the Tohoku University Global COE program titled "Global Education and Research Center for Earth and Planetary Dynamics.", and European Union FP7 CrossDrive Project. The presented analysis is based on data collected at the Subaru Telescope, which is operated by the National Astronomical Observatory of Japan (NAOJ). We express our thanks to Dr. T.S. Pyo and Dr. Y. Minowa for their kind advice and helpful support for the operation of IRCS. ASI funds PFS activities in the context of Italian participation in the ESA Mars Express mission. E. Millour and F. Forget provided the Mars Climate Database. We thank Dr. Kei Yoshimura for his useful suggestions on HDO/H_2O isotopic fractionation during the sublimation-condensation process.

References

Appéré, T., Schmitt, B., Langevin, Y., Douté, S., Pommerol, A., Forget, F., Spiga, A., Gondet, B., Bibring, J.-P., 2011. Winter and spring evolution of northern seasonal deposits on Mars from OMEGA on Mars Express. J. Geophys. Res. 116, E05001.

Benson, J.L., Kass, D.M., Kleinböhl, A., 2011. Mar's north polar hood as observed by the Mars Climate Sounder. J. Geophys. Res. 116, E03008.

Boyton, W.V., Feldman, W.C., Squyes, S.W., Prettyman, T.H., Brükner, J., Evans, L.G., Reedy, R.C., Starr, R., Annold, J.R., Drake, D.M., Englert, P.A.J., Metzger, A.E., Mitrofanov, I., Trombka, J.I., d'Uston, C., Wänke, H., Gasnault, O., Hamara, D.K., Janes, D.M., Marcialis, R.L., Maurice, S., Mikheeva, I., Taylor, G.J., Tokar, R., Shinohara, C., 2002. Distribution of hydrogen in the near surface of Mars: evidence for subsurface ice deposits. Science 297, 81.

Christensen, P.R., Bandfield, J.L., Hamilton, V.E., Ruff, S.W., Kieffer, H.H., Titus, T.N., Malin, M.C., Morris, R.V., Lane, M.D., Clark, R.L., Jakosky, B.M., Mellon, M.T., Pearl, J.C., Conrath, B.J., Smith, M.D., Clancy, R.T., Kuzmin, R.O., Roush, T., Mehall, G.L., Gorelick, N., Bender, K., Murray, K., Dason, S., Greene, E., Silverman, S., Greenfield, M., 2001. The Mars Global Surveyor Thermal Emission Spectrometer experiment: Investigation description and surface science results. J. Geophys. Res. 106, 23823–23871.

Encrenaz, T., Greathouse, T.K., Bézard, B., Fouchet, T., Lefèvre, F., Montmessin, F., Bitner, M., Kruger, A., Richter, M.J., Lacy, J.H., Forget, F., Atreya, S.K., 2010. Water vapor map of Mars near summer solstice using ground-based infrared spectroscopy. A&A 520. A33.

Engleman, R. Jr., Hinkle, K.H., Wallace, L., 2003. The near-infrared spectrum of a Th/Ar hollow cathode lamp. J. Quant. Spectrosc. Radiat. Transfer 78, 1–30.

Farmer, C.B., Davies, D.W., Holland, A.L., Laporte, D.D., Doms, P.E., 1977. Mars: Water vapor observations from the Viking orbiters. J. Geophys. Res. 82, 4225–4248.

Fedorova, A., Korablev, O., Bertaux, J.-L., Rodin, A., Kiselev, A., Perrier, S., 2006. Mars water vapor abundance from SPICAM IR spectrometer: Seasonal and geographic distributions. J. Geophys. Res. 111, E09S08.

Feldman, W. C., Prettyman, T.H., Maurice, S., Plaut, J.J., Bish, D.L., Vaniman, D.T., Mellon, M.T., Metzger, A.E., Squyres, S.W., Karunatillake, S., Boynton, W.V., Elphic, R.C., Funsten, H.O., Lawrence, D.J., Tokar, R.L., 2004. Global distribution of near-surface hydrogen on Mars. J. Geophys. Res. 109, E09006.

Fisher, D.A, 2007. Mars' water isotope (D/H) history in the strata of the Northern polar cap: inferences about the water cycle. Icarus, 187, 430-441.

Fisher, D.A, Novak, R., Mumma, M.J., 2008. D/H ratio during the northern polar summer and what the Phoenix mission might measure. J. Geophys. Res. 113, E00A15.

Formisano, V., Angrilli, F., Arnold, G., Atreya, S., Bianchini, G., Biondi, D., Blanco, A., Blecka, M.I., Coradini, A., Colangeli, L., Ekonomov, A., Esposito, F., Fonti, S., Giuranna, M., Grassi, D., Gnedykh, V., Grigoriev, A., Hansen, G., Hirsh, H., Khatuntsev, I., Kiselev, A., Ignatiev, N., Jurewicz, A., Lellouch, E., Lopez Moreno, J., Marten, A., Mattana, A., Maturilli, A., Mencarelli, E., Michalska, M., Moroz, V., Moshkin, B., Nespoli, F., Nikolsky, Y., Orfei, R., Orleanski, P., Orofino, V., Palomba, E., Patsaev, D., Piccioni, G., Rataj, M., Rodrigo, R., Rodriguez, J., Rossi, M., Saggin, B., Titov, D., Zasova, L., 2005. The Planetary Fourier Spectrometer (PFS) onboard the European Mars Express mission. Planet. Space Sci. 53, 10, 963–974.

Fouchet, T., Lellouch, E, 2000. Vapor pressure isotope fractionation effects in planetary atmospheres: Application to deuterium. Icarus 144, 114–123.

Fouchet, T., Lellouch, E., Ignatiev, N.I., Forget, F., Titov, D.V., Tschimmel, M., Montmessin, F., Formisano, V., Giuranna, M., Maturilli, A., Encrenaz, T., 2007. Martian water vapor: Mars Express PFS/LW observations. Icarus 190, 32–49.

Frankenberg, C., Yoshimura, K., Warneke, T., Aben, I., Butz, A., Deutscher, N., Grif- fith, D., Hase, F., Notholt, J., Schneider, M., Schrijver, H., Röckmann, T., 2009. Dynamic Processes Governing Lower-Tropospheric HDO/H_2O Ratios as Observed from Space and Ground. Science 325, 1374.

Gamache, R., Kennedy, S., Hawkins, R., Rothman, L., 2000. Total internal partition sums for molecules in terrestrial atmosphere. J. Molecular Structure 517–518, 407–425.

Hase, F., Wallace, L., McLeod, S.D., Harrison, J.J., Bernath, P.F., 2010. The ACE–FTS atlas of the infrared solar spectrum. J. Quant. Spectrosc. Radiat. Transfer 111, 521–528.

Ignatiev, N.I., Grassi, D., Zasova, L.V., 2005. Planetary Fourier spectrometer data analysis: fast radiative transfer models. Planet. Space Sci. 53, 1035–1042.

Kobayashi, N., Tokunaga, A., Terada, H., Goto, M., Weber, M., Potter R., Onaka, P., Ching, G., Young, T., Fletcher, K., Neil, D., Robertson, L., Cook, D., Imanishi, M., Warren, D., 2000. IRCS: Infrared Camera and Spectrograph for the Subaru Telescope. In Proc. SPIE 4008: Optical and IR Telescope Instrumentation and Detectors, eds M. Iye & A. F. Moorwood, 1056.

Krasnopolsky, V.A., Bjoraker, G.L. Mumma, M.J., Jennings, D.E., 1997. High-resolution spectroscopy of Mars at 3.7 and 8 μm: A sensitive search of H_2O_2, H_2CO, HCl, and CH_4, and detection of HDO. J. Geophys. Res. 102(E3), 6525–6534.

Krasnopolsky, V.A, Maillard, J.P, Owen, T.C., 2004. Detection of methane in the Martian atmosphere: evidence for life? Icarus 172, 53747.

Maltagliati, L., Titov, D.V., Encrenaz, T., Melchiorri, R., Forget, F., Garcia-Comas, M., Keller, H.U., Langevin, Y., Bibring, J.-P., 2008. Observations of atmospheric water vapor above the Tharsis volcanoes on Mars with the OMEGA/MEx imaging spectrometer. Icarus 194, 53–64.

Montmessin, F., Forget, F., Rannou, P., Cabane, M., Haberle, R.M., 2004. Origin and role of water ice clouds in the Martian water cycle as inferred from a general circulation model. J. Geophys. Res. 109, 10004.

Montmessin, F., Fouchet, T., Forget, F., 2005. Modeling the annual cycle of HDO in the Martian atmosphere. J. Geophys. Res. 110, E03006.

Moores, J.E., Brown, R.H., Lauretta, D.S., Smith, P.H., 2012. Experimental and theoretical simulation of sublimating dusty water ice with implications for D/H ratios of water ice on Comets and Mars. Planetary Science, 1, 1.

Mumma, M.J., Novak, R.E., DiSanti, M.A., Bonev, B., Dello Russo N., Magee-Sauer, K., 2003. Seasonal mapping of HDO and H_2O, in Sixth International Conference on Mars Atmosphere, Abstract 3186, Jet Pro- pul. Lab., Pasadena, Calif.

Novak, R.E., Mumma, M.J., Villanueva, G.L., 2011. Measurement of the isotopic signatures of water on Mars; implications for studying methane. Planetary Space Science 59, 163–8.

Novak, R.E., Mumma, M.J., Villanueva, G.L., 2014. Diurnal mapping of [H_2O], [HDO], [HDO]/[H_2O], and $O_2(a^1\Delta_g)$ emission on Mars using ground based high-resolution spectroscopy, The 5th International Workshop on the Mars Atmosphere: Modeling and Observation, id.3402.

Owen, T., Maillard, J.P., de Bergh, C., Lutz, B.L., 1988. Deuterium on Mars: The abundance of

HDO and the value of D/H. Science 240, 1767–1770.

Pankine, A.A., Tamppari, L.K., Smith, M.D., 2010. MGS TES observations of the water vapor above the seasonal and perennial ice caps during northern spring and summer. Icarus 210, 58–71.

Pankine A.A, Tamppari L.K., 2015. Constrains on water vapor vertical distribution at the Phoenix landing site during summer from MGS TES day and night observations. Icarus, 252, 107-120.

Rothman, L.S., Rinsland, C.P., Goldman, A., Massie, S.T., Edwards, D.P., Flaud, J.-M., Perrin, A., Camy-Peyret, C., Dana, V., Mandin, J.-Y., Schroeder, J., McCann, A., Gamache, R.R., Wattson, R.B., Yoshino, K., Chance, K.V., Jucks, K.W., Brown, L.R., Nemtchinov, V., Varanasi, P., 1998. The HITRAN molecular spectroscopic database and HAWKS (HITRAN Atmospheric Workstation): 1996 Edition. J. Quant. Spectrosc. Radiat. Transfer 60, 665–710.

Rothman, L.S., Gordon, I.E., Barbe, A., Chris Benner, D., Bernath, P.F., Birk, M., Boudon, V., Brown, L.R, Campargue, A., Champion, J.-P., Chance, K., Coudert, L.H., Dana, V., Devi, V.M., Fally, S., Flaud, J.-M., Gamache, R.R., Goldman, A., Jacquemart, D., Kleiner, I., Lacome, N., Lafferty, W.J., Mandin, J.-Y., Massie, S.T., Mikhailenko, S.N., Miller, C.E., Moazzen-Ahmadi, N., Naumenko, O.V., Nikitin, A.V., Orphal, J., Perevalov, V.I., Perrin, A., Predoi-Cross, A., Rinsland, C.P., Rotger, M., Simeckova, M., Smith, M.A.H., Sung, K., Tashkun, S.A., Tennyson, J., Toth, R.A., Vandaele, A.C., Vander Auwera, J., 2009. The HITRAN 2008 molecular spectroscopic database. J. Quant. Spectrosc. Radiat. Transfer 110, 533–572.

Sindoni, G., Formisano, V., Geminale, A., 2011. Observations of water vapour and carbon monoxide in the Martian atmosphere with the SWC of PFS/MEX. Planet. Space Sci. 59, 149–162.

Smith, M.D., 2002. The annual cycle of water vapor on Mars as observed by the Thermal Emission Spectrometer. J. Geophys. Res. 107, E11.

Smith, M.D., 2004. Interannual variability in TES atmospheric observations of Mars during 1999–2003. Icarus 167, 148–165.

Smith, M.D., Wolff, M.J., Clancy, R.T., Murchie, S.L., 2009a. Compact Reconnaissance Imaging Spectrometer observations of water vapor and carbon monoxide. J. Geophys. Res. 114, E00D03.

Smith, P. H., Tamppari, L.K., Arvidson, R.E., Bass, D., Blaney, D., Boynton, W.V., Carswell, A., Catling, D.C., Clark, B.C., Duck, T., DeJong, E., Fisher, D., Goetz, W., Gunnlaugsson, H.P., Hecht, M.H., Hipkin, V., Hoffman, J., Hviid, S.F., Keller, H.U., Kounaves, S.P., Lange, C.F., Lemmon, M.T., Madsen, M.B., Markiewicz, W.J., Marshall, J., McKay, C.P., Mellon, M.T., Ming, D.W., Morris, R.V., Pike, W.T., Renno, N., Staufer, U., Stoker, C., Taylor, P., Whiteway, J.A., Zent A.P., 2009b. H_2O at the Phoenix Landing site. Science 325, 58-61.

Spinrad, H., Münch, G., Kaplan, L.D., 1963. Letter to the Editor: The detection of water vapor on

Mars. Astrophys. J. 137, 1319–1321.

Vandaele, A.C., Daerden, F., Drummond, R., Neefs. E., López-Moreno, J.-J., Rodriguez Gomez, J., Patel. M. R., Bellucci, G., the NOMAD team, 2011. NOMAD, a spectrometer suite for nadir and solar occultation observations on the ExoMars Trace Gas Orbiter. Proceedings of The Fourth International Workshop on the Mars Atmosphere: Modelling and observation, pp 484-487.

Tschimmel, M., Ignatiev, N.I., Titov, D., Lellouch, E., Fouchet, T., Giuranna, M., Formisano, V., 2008. Investigation of the water vapour on Mars with PFS/SW of Mars Express. Icarus 195, 557–575.

Trokhimovskiy, A., Feforova, A., Korablev, O., Montmessin, F., Bertaux, J.-L., Rodin, A., Smith, M.D., 2015. Mars' water vapor mapping by the SPICAM IR spectrometer: Five martian years of observations. Icarus, 251, 50-64.

Villanueva, G.L., Mumma, M.J., Novak, R.E., Hewagama, T., Bonev, B.P., DiSanti, M.A., 2008. Mapping the D/H of water on Mars using high-resolution spectroscopy. Proceedings of the Third International Workshop on the Mars Atmosphere, LPI Co 1447, p. 9101.

Villanueva, G.L., Mumma, M.J., Novak, R.E., 2013. Hydrogen, oxygen, and carbon isotopic ratios in the Martian atmosphere. Proceedings of the 44th Lunar and Planetary Science Conference, LPI Contribution No. 1719, p. 2551

Villanueva, G.L., Mumma, M.J., Novak, R.E., Käufl, H.U., Hartogh, P., Encrenaz, T., Tokunaga, A., Khayat, A., Smith, M.D., 2015. Strong water isotopic anomalies in the martian atmosphere: Probing current and ancient reservoirs. Science, 348, 218-221.

Webster, C.R., Mahaffy, P.R., Flesch, G.J., Niles, P.B., Jones, J.H., Leshin, L.A., Atreya, S.K., Stern, J.C., Christensen, L.E., Owen, T., Franz, H., Pepin, R.O., Steele, A., MSL Science Team, 2013. Isotope ratio of H, C, and O in CO_2 and H_2O of the Martian atmosphere. Science 341, 260.

Appendices

Appendix A. Retrieval of Instrumental line shape of IRCS

Since line widths of the Martian H_2O and HDO lines are ~10 times smaller than the spectral resolution of IRCS, the observed line shapes reflect the instrumental line shape (ILS) of IRCS. Therefore, characterization of the ILS is important to perform retrieval accurately. Here, we retrieved the ILS using Ar lamp measurements carried out in a similar configuration to the Mars observation. The lamp measurements were performed for 2.5 h in order to obtain sufficient signal to noise ratio. Line widths of Ar lamps are so narrow (~0.02 cm^{-1}, Engleman et al., 2003) that the observed line shapes represent the ILS of IRCS. There are five independent lines in the measured spectral ranges (3016.7336 cm^{-1}, 3023.0817 cm^{-1}, 3040.5647 cm^{-1}, 3191.5201 cm^{-1}, and 3272.9622 cm^{-1}), and we used lines at 3040.5647 cm^{-1}, 3191.5201 cm^{-1}, and 3272.9622 cm^{-1} for retrieval of the ILS. **Figure A-1** shows all the measurements for the three lines. We found that full width at half maximum (FWHM) of the ILS is not constant but depends on pixel position on the detector.

We attempted to retrieve the ILS as a function of FWHM. As the first attempt, Gaussian and sinc-squared functions were applied to fit these data since these functions are well known as a line shape of eschelle spectroscopy. However, as shown in **Fig. A-2**, both functions could not reproduce the observed line shape, especially in the wings. Therefore, we assumed that the ILS is a combination of two functions, one for line center and the other for wings. We tested the six cases listed in **Table A-1** and determined the most accurate one by using the least squares method. We derived the switching spectral point of the two functions and the relationship between their FWHMs in the retrieval process.

As shown in **Table A-1,** the combination of two Gaussian functions is most accurate for the ILS of IRCS. The retrieved ILS of IRCS is given by

$$ILS(x) = \begin{cases} F_1(x) & (|x - x_0| \leq 1.9\, pixels) \\ F_2(x) & (|x - x_0| > 1.9\, pixels) \end{cases},$$

where

$$F_1(x) = \exp(-(\frac{x - x_0}{w_{ILS}})^2/2), \quad F_2(x) = \beta \times \exp(-(\frac{x - x_0}{w'_{ILS}})^2/2),$$

$$w'_{ILS} = w_{ILS} \times 1.72, \quad \beta = F_1(1.9) / \exp(-(1.9 / w_{ILS})^2 / 2).$$

w_{ILS} and w'_{ILS} are FWHM of the Gaussian functions. The FWHM of the second function (for line wing) is 1.72 times larger than that of the first function (for line center). The two functions are switched at the 1.9 pixel far from the observed wavelength. **Figure A-3** shows the Ar lamp measurements and the retrieved ILS. The IRCS could reproduce the wings of the lamp spectra much better than simple Gaussian or sinc-squared function (**Fig. A-2**).

Figure captions

Figure 1. Example of a spectrum obtained by IRCS. Five spectral bands can be observed simultaneously: 2.94–3.01 μm (order-19), 3.01–3.18 μm (order-18), 3.28–3.36 μm (order-17), 3.49–3.57 μm (order-16), and 3.72–3.81 μm (order-15). The spectrum was observed on January 5 with 5-min integration and without binning. Circular symbols in (c) represent CH_4 lines and the other features in Order-17 are H_2O lines. Triangle symbols in (e) represent the HDO lines. The gray boxes represent the spectral ranges used in this analysis.

Figure 2. Rate of surface radiation in the observed IRCS signals at HDO spectral range. Differences in colors show the observing latitudes or longitudes.

Figure 3. Examples of the fitting analysis with Mars (top) and standard star (bottom) H_2O lines. In the upper spectra at each panel, the IRCS data are shown in black and the best-fit synthetic spectra with and without Martian contributions are in red and blue, respectively. The bottom spectra show residual spectra after removing the terrestrial contributions (Black: IRCS data, Red: the best-fit spectra). The Martian spectra were measured on January 5, 2012 over the latitude 35°N. Retrieved column densities of Martian H_2O are 8 (±2) pr-μm from 3035 cm^{-1} ranges and 11 (±1) pr-μm from 3216 cm^{-1} ranges (1 pr-μm equals 3.34×10^{18} molecules/cm^2).

Figure 4. Same as Fig. 3, but for HDO lines. Retrieved column densities of Martian HDO are 16 (±4) pr-nm from 2677 cm^{-1} ranges and 12 (±3) pr-nm from 2672 cm^{-1} ranges.

Figure 5. An example of retrieval of H_2O abundance from PFS/SWC data at 13.3°N. The black curve shows the averaged PFS spectrum and the red one represents the best-fit synthetic spectrum. The retrieved H_2O mixing ratio is 150 ± 28 ppm. The uncertainty in the retrieved H_2O mixing ratio is about 19% total (Sindoni et al., 2011).

Figure 6. (Left) Latitudinal distribution of H_2O abundances measured by Subaru/IRCS. (Middle) Latitudinal distribution of H_2O abundances predicted by the Mars Climate Database (ver5.0). (Right) Latitudinal distribution of HDO abundances measured by Subaru/IRCS. Differences in colors show the observing longitudes. The values are divided by (P_{surf}/6.1) to remove the effect of topography, where P_{surf} is surface pressure in mbar. The horizontal bars show the estimated error values and the vertical bars represent the latitudinal footprints of the binned 10 pixels.

Figure 7. (Left) Latitudinal distribution of the HDO/H_2O ratio (relative value to VSMOW) measured by Subaru/IRCS. Differences in color represent the observed longitudes. The horizontal bars show the estimated error values and the vertical bars represent the latitudinal footprints of the binned 10 pixels. (Right) Latitudinal mean values of the HDO/H_2O ratios are shown in the top panel. The error bars correspond to standard deviations. The triangle symbols show the predicted values by GCM of Montmessin et al. (2005). The values are extracted from the zonal averaged map of the HDO/H_2O ratio shown in **Fig. 2** of Montmessin et al. (2005).

Figure 8: (Left) Latitudinal distribution of the H_2O column density retrieved from MEX/PFS–SWC observations. The light blue, blue, yellow, and green curves represent orbit10542

(16°W, 10/April), orbit10547 (167°W, 12/April), orbit10542 (162°W, 14/April), and orbit10542 (109°W, 14/April), respectively. The red curve corresponds to the longitudinal mean profile and the error bars represent standard deviation. The black points show the H_2O column density at *Ls* = 52° (northern spring) retrieved by Subaru/IRCS. (Right) Latitudinal distribution of the HDO column density retrieved from Subaru/IRCS observations. The red and black points represent the values at *Ls* = 96° (northern summer) and *Ls* = 52° (northern spring), respectively. The blue curve denotes the longitudinal mean profile of the retrieved HDO column density at *Ls* = 96° and the error bars represent standard deviation. These values have been normalized by surface pressure in order to remove the effect of topography.

Figure 9: Seasonal variation of the HDO/H_2O ratio (relative to VSMOW). The red curve represents the distribution observed at *Ls* = 96° and the black curve indicates the distribution at *Ls* = 52° (similar to the right panel of **Fig. 7**). The error values of the HDO/H_2O ratio at *Ls* = 96° are estimated from standard deviations of both H_2O and HDO mixing ratios. ~~The values are extracted from the zonal averaged map of the HDO/H_2O ratio shown in Fig. 2 of Montmessin et al. (2005).~~

Figure 10. (Top) Longitudinal distribution of H_2O column abundances. (Bottom) Longitudinal

distribution of HDO column abundances. Differences in colors represent the observing latitudes. The values are divided by (P_{surf}/6.1) to remove the effect of topography, where P_{surf} is surface pressure in mbar. The vertical bars denote the estimated error values and the horizontal bars represent the longitudinal footprints of the binned 10 pixels.

Figure 11. (Top) Longitudinal distribution of the HDO/H_2O ratio (relative value to VSMOW; HDO/H_2O = 3.11×10^{-4}). Differences in colors signify the observing latitudes. The vertical bars show the estimated error values and the horizontal bars represent the longitudinal footprints of the binned 10 pixels. (Bottom) Latitudinal-mean values of the HDO/H_2O ratios shown in the top panel. The error bars correspond to their standard deviations.

Figure 12. (Top) Local time distribution of H_2O column abundances. (Bottom) Local time distribution of HDO column abundances. Differences in colors represent the observing latitudes.

Figure 13. (Top) Local time distribution of the HDO/H_2O ratio. Differences in colors denote the observing latitudes. (Bottom) Latitudinal mean values of the HDO/H_2O ratios shown in the top panel. The error bars correspond to their standard deviations.

Figure 14. HDO/H_2O ratio with H_2O column density from our measurements at *Ls*=96° (left) and *Ls*=52° (right).

Figure 15. Sublimation–condensation process in the Martian water cycle and the HDO/H_2O ratio in water vapor during the northern spring (*Ls* = 52°) and summer (*Ls* = 96°), inferred from our observations

Figure A-1. Ar lamp spectra measured by IRCS at 3049.5647 cm^{-1} (left), 3191.5201 cm^{-1} (center), and 3272.9622 cm^{-1} (right). All observed data (all pixels in the slit) are shown together.

Figure A-2. Ar lamp spectra shown in Figure A-1 and their best-fit spectra with Gaussian function (red curves) and Sinc-squared function (blue curves).

Figure A-3. Ar lamp spectra shown in Figure A-1 and the retrieved ILS by combination of two Gaussian functions (red curves).

Tables

Table 1 Parameters of Mars observations with Subaru/IRCS

Date and time (UT)	*Ls* (°)	MY	Doppler shift (km/s)	Diameter (″)	Airmass	Slit direction	Observing areas (°)	Local Time
4/January/2012 13:12–16:26	52.4	31	-15	9.3	1.14–1.09	E–W	0N–40N	10–17
5/January/2012 12:34–16:28	52.9	31	-15	9.4	1.25–1.10	N–S	256W–302W	13–15
13/April/2012 8:24–10:49	96.2	31	+11	11.5	1.05–1.56	N–S	34W–60W	9–10

Table 2 PFS orbits used for the joint observation with Subaru/IRCS

Orbit number	Date (UT)	Longitude	Local time
#10542	10/April/2012 12:21–13:20	16°W	16 h
#10547	11/Aprli/2012 23:08–24:06	167°W	16 h
#10554	13/April/2012 23:47–25:14	162°W	16 h
#10557	14/April/2012 20:45–22:12	109°W	16 h

Table 3 Parameters of HDO and H_2O lines used in this study. The values are taken from the HITRAN 2008 spectroscopic database (Rothman et al., 2009).

Molecular	H_2O	H_2O	HDO	HDO
Wavenumber [cm^{-1}]	3035.78356	3216.52218	2672.59294	2677.71967
Intensity [cm] (for 296 K)	3.219×10^{-22}	2.848×10^{-22}	7.463×10^{-24}	9.117×10^{-24}
Lower state Energy [cm^{-1}]	446.6966	222.0528	116.4613	91.3302

Air-broadened half-width [cm^{-1} atm^{-1}] (for modeling of terrestrial lines)	0.0702	0.1080	0.0969	0.0975
Temperature-dependence exponent for the half-width	0.32	0.76	0.77	0.77

Table A1. List of combinations tested in retrieval of the ILS

	1st function (for line center)	2nd function (for line wing)	Chi-square (relative values)
Case-1	Gauss	Gauss	1.00
Case-2	Lorenz	Lorenz	5.19
Case-3	Gauss	Lorenz	1.38
Case-4	Lorenz	Gauss	5.17
Case-5	Sinc	Gauss	2.31
Case-6	Sinc	Lorenz	2.43

Figure1

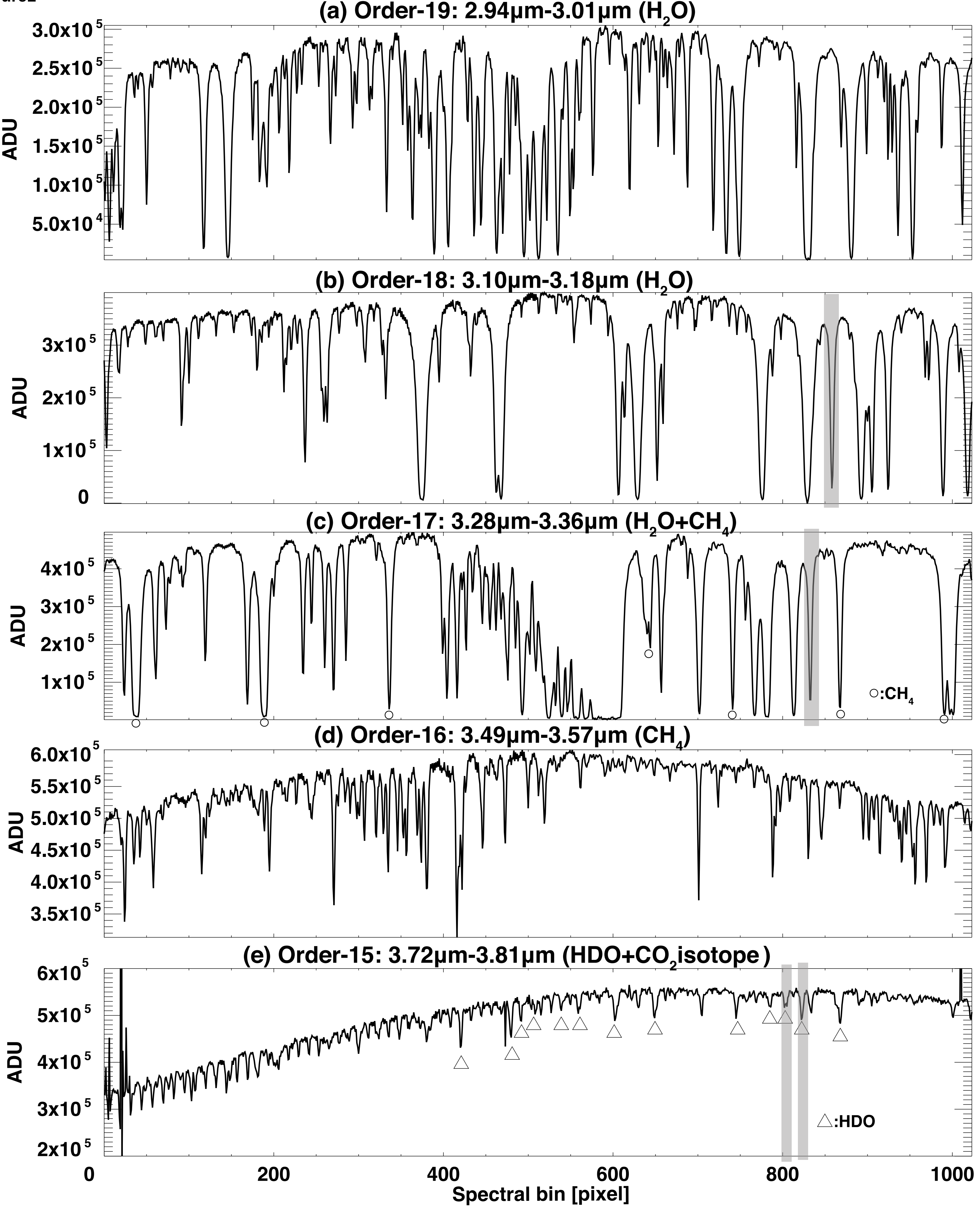
(a) Order-19: 2.94μm-3.01μm (H2O)
ADU
3.0x10^5
2.5x10^5
2.0x10^5
1.5x10^5
1.0x10^5
5.0x10^4
(b) Order-18: 3.10μm-3.18μm (H2O)
ADU
3x10^5
2x10^5
1x10^5
0
(c) Order-17: 3.28μm-3.36μm (H2O+CH4)
ADU
4x10^5
3x10^5
2x10^5
1x10^5
○:CH4
(d) Order-16: 3.49μm-3.57μm (CH4)
ADU
6.0x10^5
5.5x10^5
5.0x10^5
4.5x10^5
4.0x10^5
3.5x10^5
(e) Order-15: 3.72μm-3.81μm (HDO+CO2isotope)
ADU
6x10^5
5x10^5
4x10^5
3x10^5
2x10^5
△:HDO
0
200
400
600
800
1000
Spectral bin [pixel]

Figure2

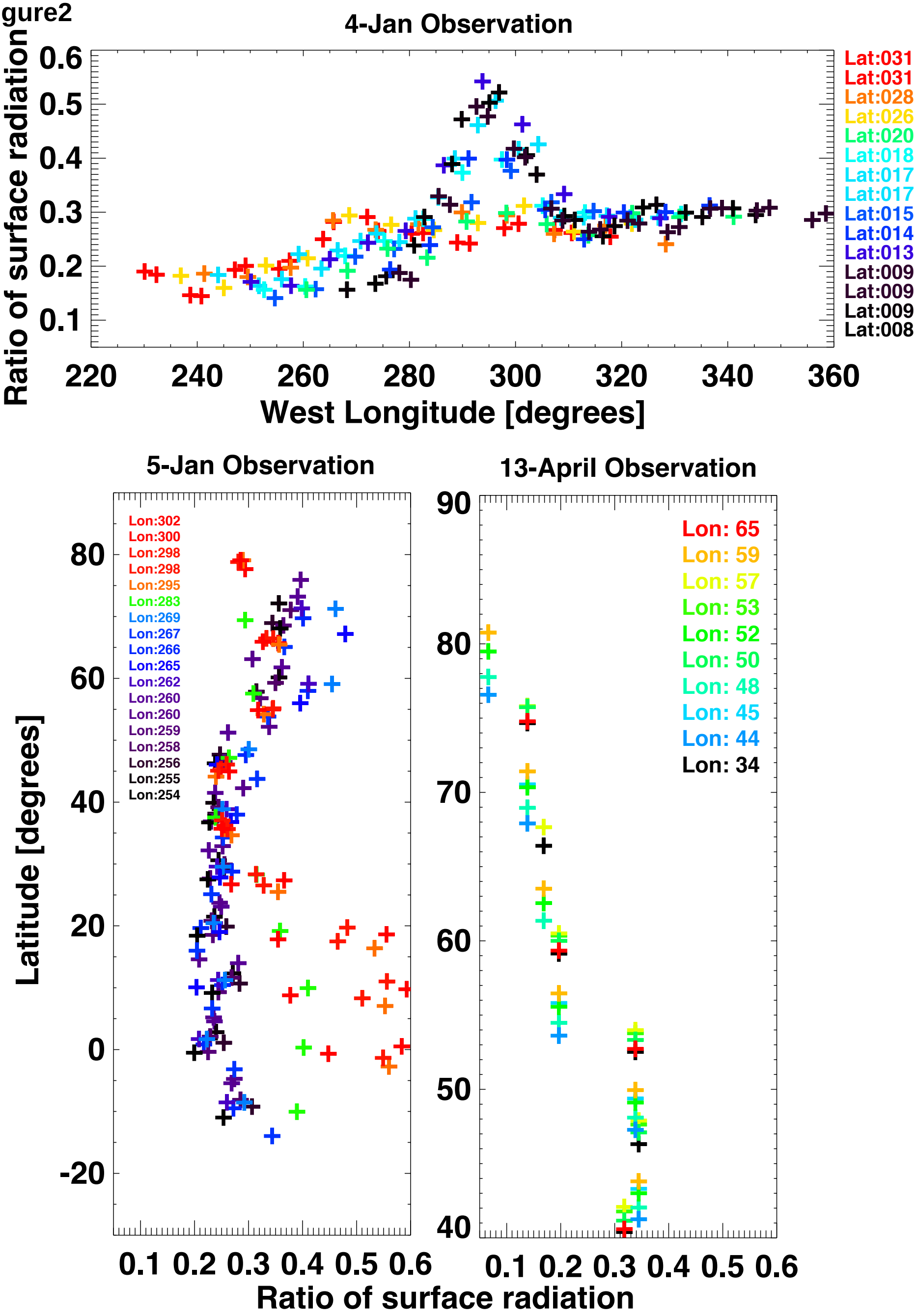
4-Jan Observation
Ratio of surface radiation
0.6
0.5
0.4
0.3
0.2
0.1
220
240
260
280
300
320
340
360
West Longitude [degrees]
Lat:031
Lat:031
Lat:028
Lat:026
Lat:020
Lat:018
Lat:017
Lat:017
Lat:015
Lat:014
Lat:013
Lat:009
Lat:009
Lat:009
Lat:008
5-Jan Observation
Latitude [degrees]
80
60
40
20
0
-20
Lon:302
Lon:300
Lon:298
Lon:298
Lon:295
Lon:283
Lon:269
Lon:267
Lon:266
Lon:265
Lon:262
Lon:260
Lon:260
Lon:259
Lon:258
Lon:256
Lon:255
Lon:254
0.1
0.2
0.3
0.4
0.5
0.6
13-April Observation
90
80
70
60
50
40
Lon: 65
Lon: 59
Lon: 57
Lon: 53
Lon: 52
Lon: 50
Lon: 48
Lon: 45
Lon: 44
Lon: 34
0.1
0.2
0.3
0.4
0.5
0.6
Ratio of surface radiation

Figure3

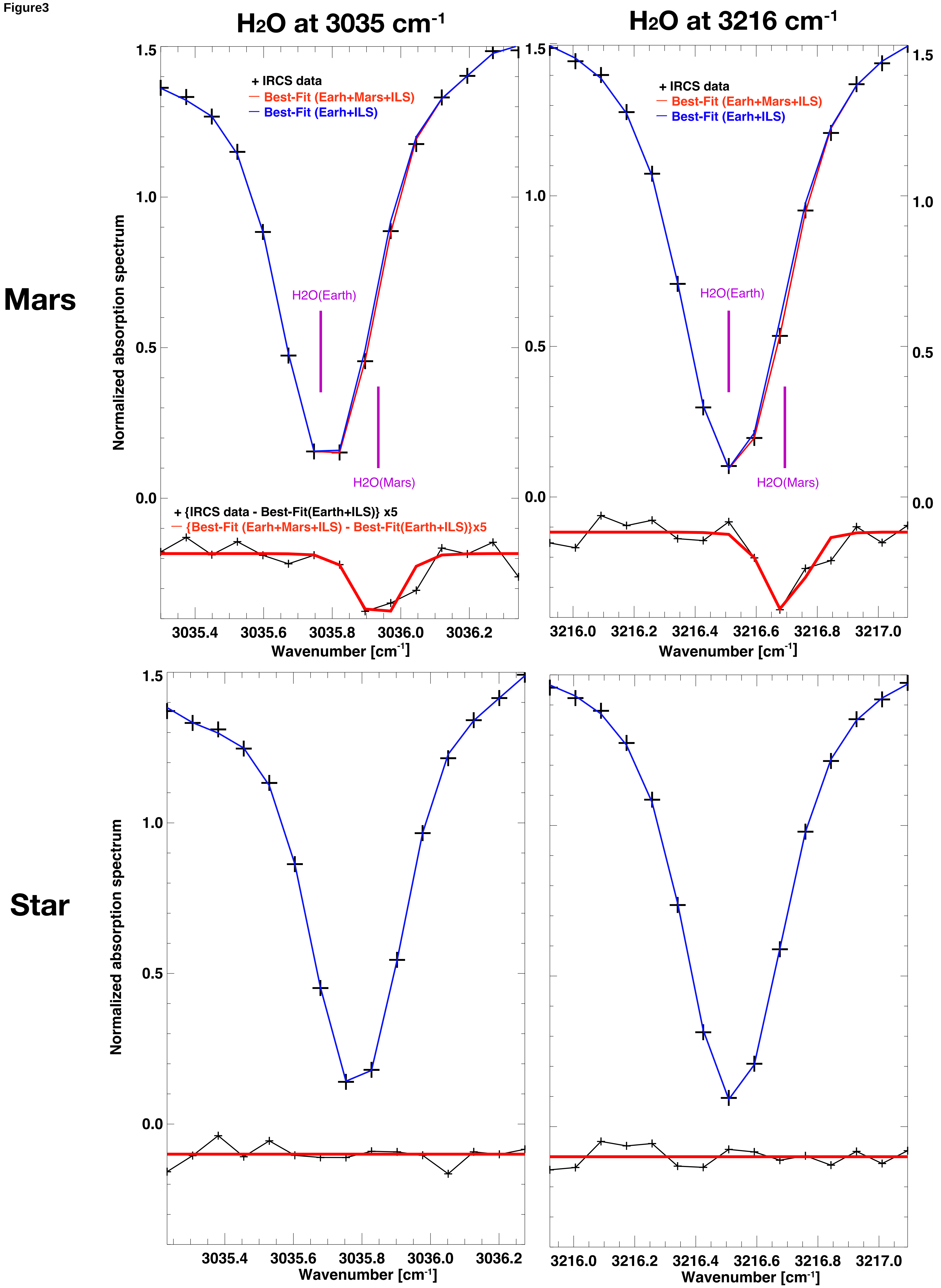
H2O at 3035 cm-1
H2O at 3216 cm-1
Mars
Star
Normalized absorption spectrum
+ IRCS data
Best-Fit (Earh+Mars+ILS)
Best-Fit (Earh+ILS)
H2O(Earth)
H2O(Mars)
+ {IRCS data - Best-Fit(Earth+ILS)} x5
{Best-Fit (Earh+Mars+ILS) - Best-Fit(Earth+ILS)}x5
0.0
0.5
1.0
1.5
3035.4
3035.6
3035.8
3036.0
3036.2
3216.0
3216.2
3216.4
3216.6
3216.8
3217.0
Wavenumber [cm-1]

Figure4

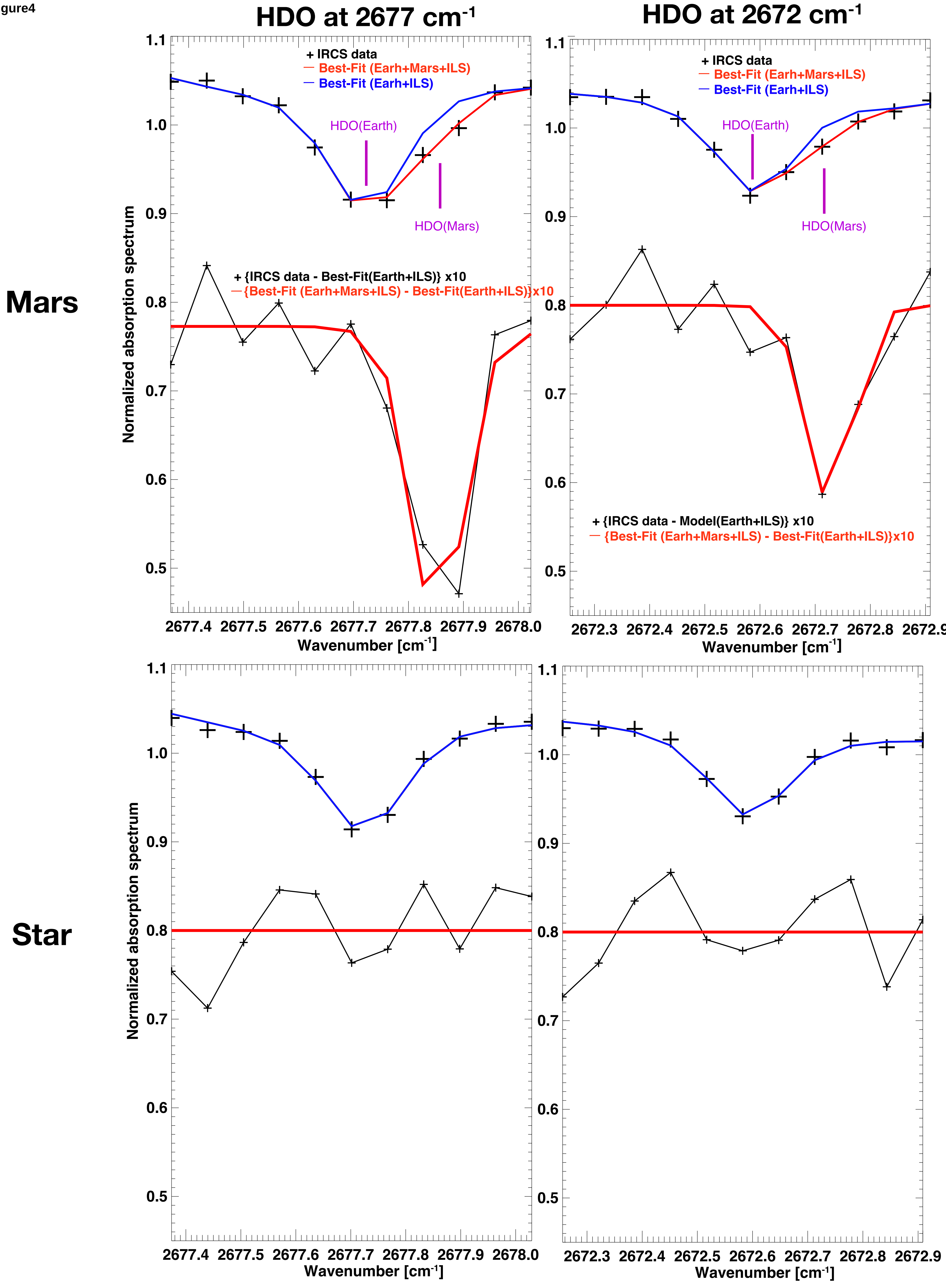
HDO at 2677 cm-1
HDO at 2672 cm-1
Mars
Star
+ IRCS data
Best-Fit (Earh+Mars+ILS)
Best-Fit (Earh+ILS)
HDO(Earth)
HDO(Mars)
+ {IRCS data - Best-Fit(Earth+ILS)} x10
{Best-Fit (Earh+Mars+ILS) - Best-Fit(Earth+ILS)}x10
+ {IRCS data - Model(Earth+ILS)} x10
Normalized absorption spectrum
1.1
1.0
0.9
0.8
0.7
0.6
0.5
2677.4
2677.5
2677.6
2677.7
2677.8
2677.9
2678.0
2672.3
2672.4
2672.5
2672.6
2672.7
2672.8
2672.9
Wavenumber [cm-1]

Figure5

Click here to download high resolution image

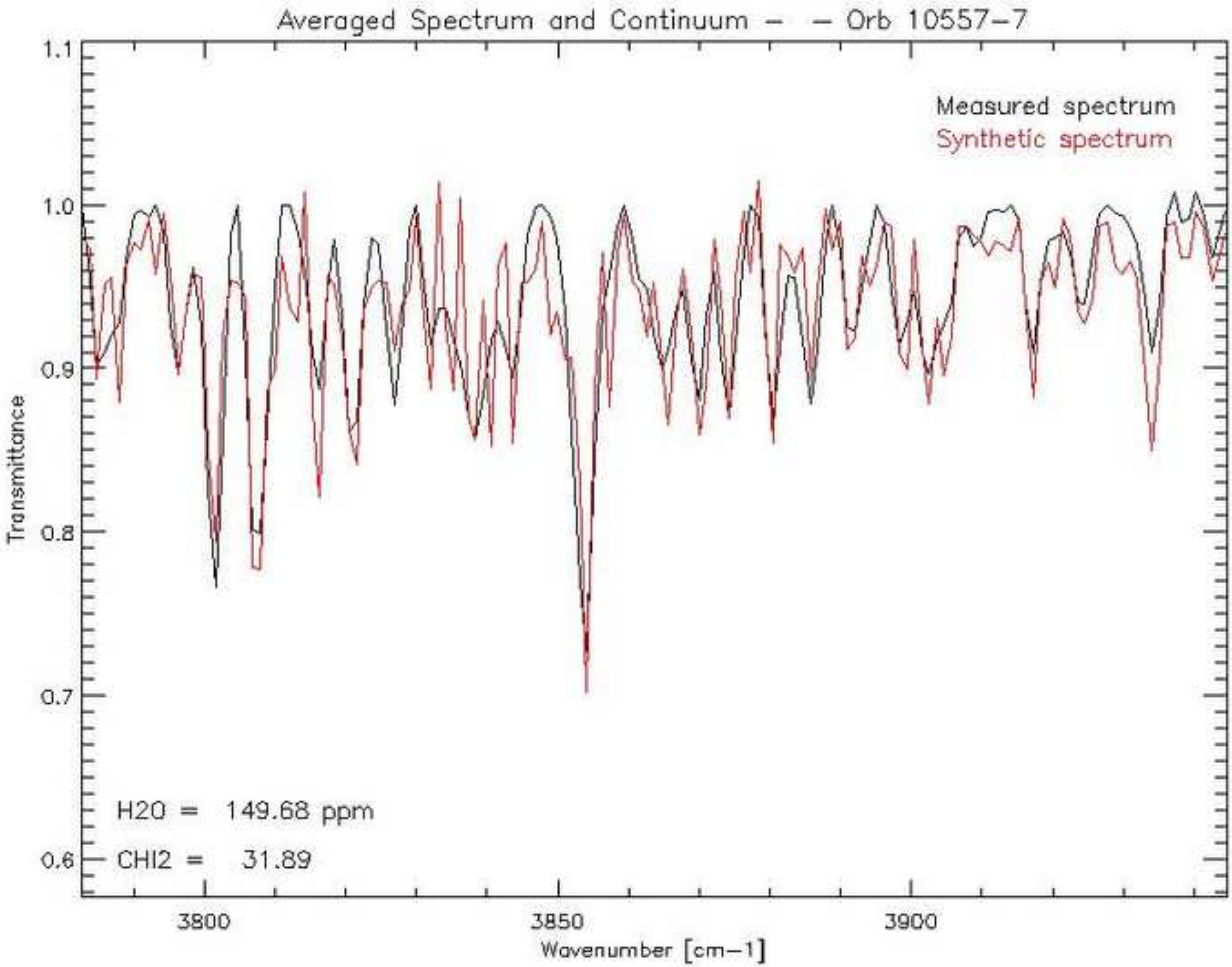

Figure6

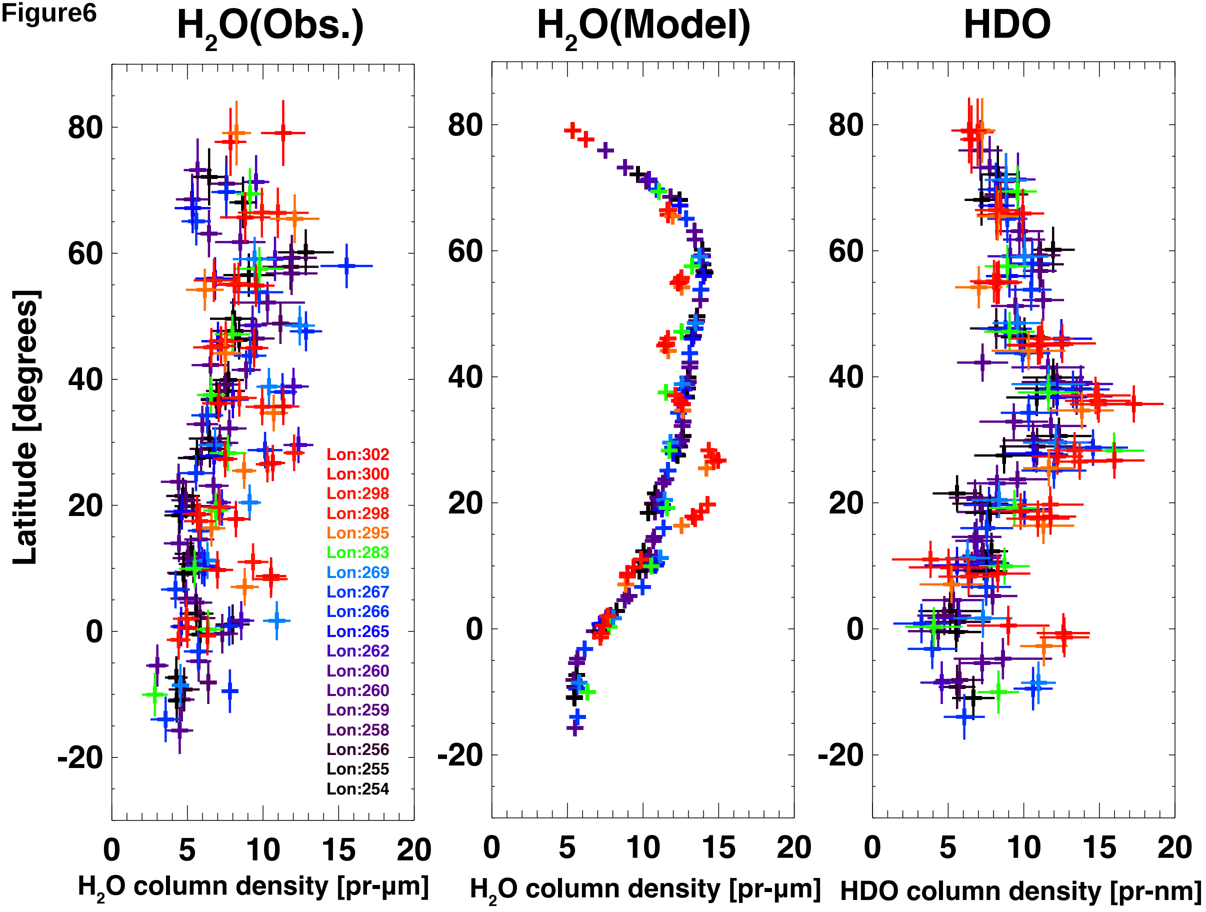
H$_2$O(Obs.)
H$_2$O(Model)
HDO
Latitude [degrees]
80
60
40
20
0
-20
0
5
10
15
20
H$_2$O column density [pr-μm]
H$_2$O column density [pr-μm]
HDO column density [pr-nm]
Lon:302
Lon:300
Lon:298
Lon:298
Lon:295
Lon:283
Lon:269
Lon:267
Lon:266
Lon:265
Lon:262
Lon:260
Lon:260
Lon:259
Lon:258
Lon:256
Lon:255
Lon:254

Figure7

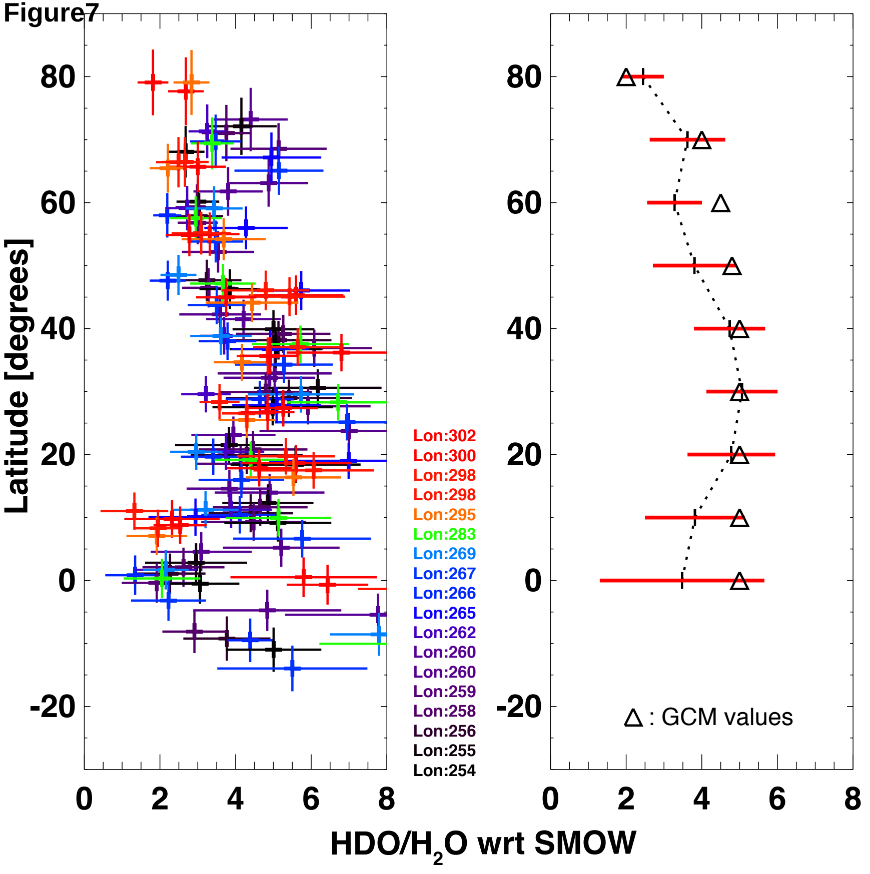
Latitude [degrees]
80
60
40
20
0
-20
0
2
4
6
8
Lon:302
Lon:300
Lon:298
Lon:298
Lon:295
Lon:283
Lon:269
Lon:267
Lon:266
Lon:265
Lon:262
Lon:260
Lon:260
Lon:259
Lon:258
Lon:256
Lon:255
Lon:254
80
60
40
20
0
-20
△ : GCM values
0
2
4
6
8
HDO/H_2O wrt SMOW

Figure8

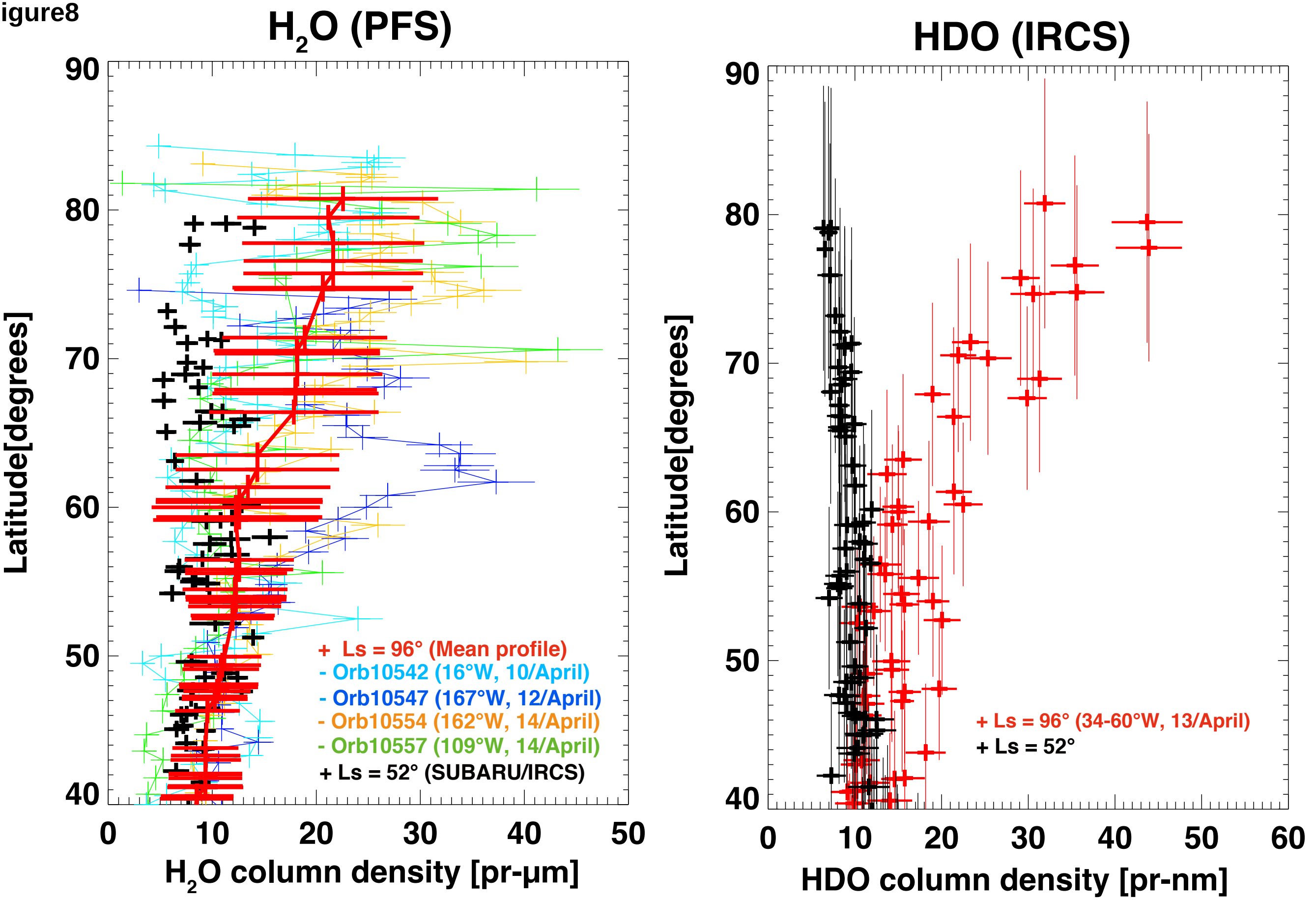
H$_2$O (PFS)
HDO (IRCS)
90
80
70
60
50
40
Latitude[degrees]
0
10
20
30
40
50
60
H$_2$O column density [pr-μm]
HDO column density [pr-nm]
+ Ls = 96° (Mean profile)
- Orb10542 (16°W, 10/April)
- Orb10547 (167°W, 12/April)
- Orb10554 (162°W, 14/April)
- Orb10557 (109°W, 14/April)
+ Ls = 52° (SUBARU/IRCS)
+ Ls = 96° (34-60°W, 13/April)
+ Ls = 52°

Figure9

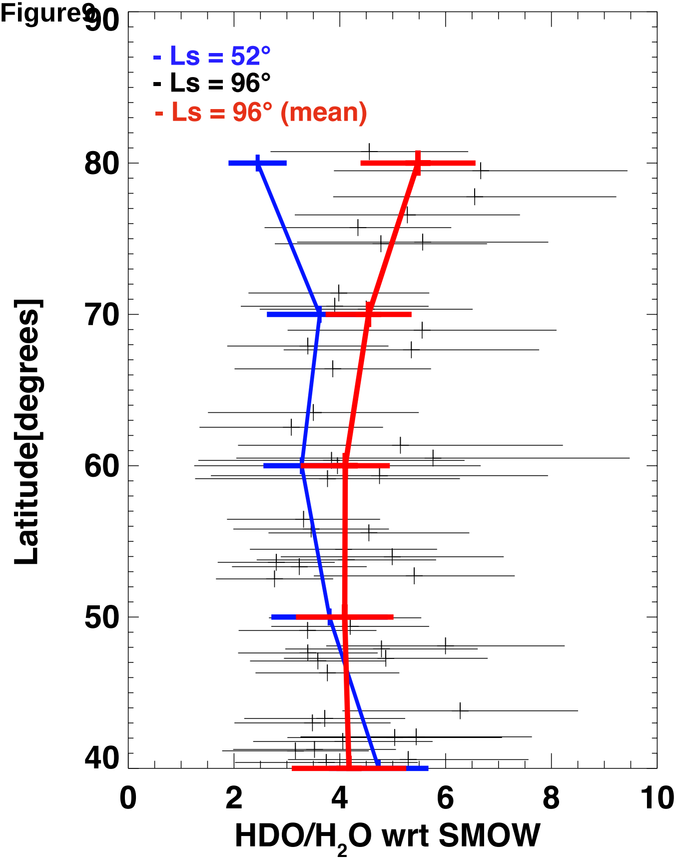

- Ls = 52°
- Ls = 96°
- Ls = 96° (mean)
90
80
70
60
50
40
Latitude[degrees]
0
2
4
6
8
10
HDO/H_2O wrt SMOW

Figure10

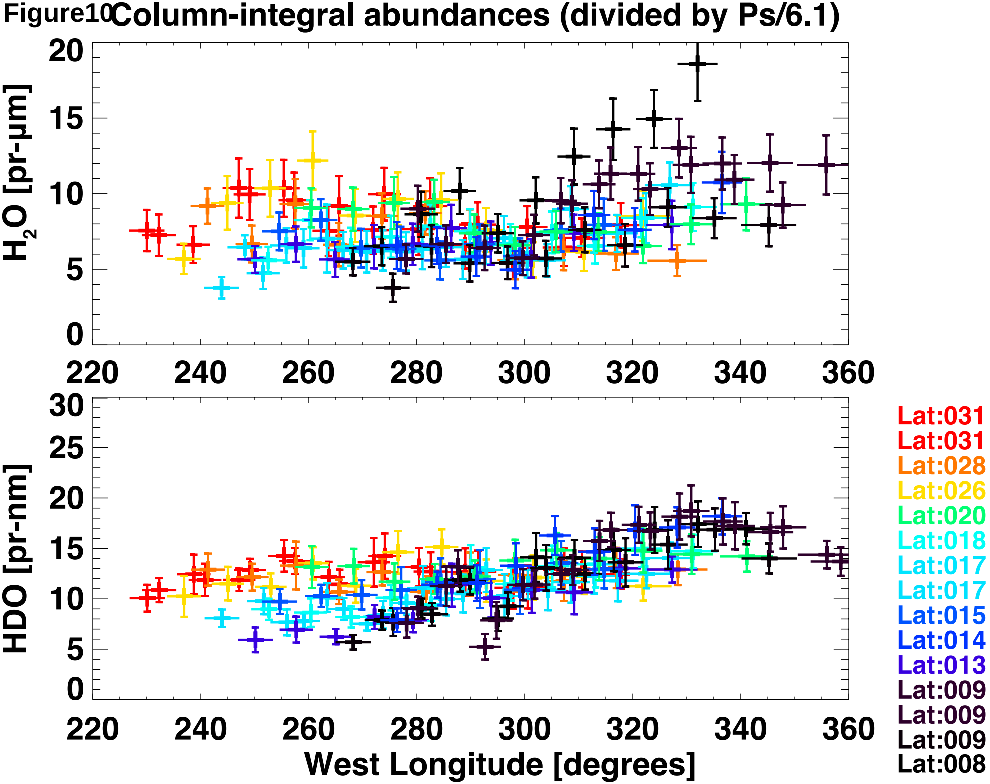
Column-integral abundances (divided by Ps/6.1)
H_2O [pr-μm]
20
15
10
5
0
220
240
260
280
300
320
340
360
HDO [pr-nm]
30
25
20
15
10
5
0
220
240
260
280
300
320
340
360
West Longitude [degrees]
Lat:031
Lat:031
Lat:028
Lat:026
Lat:020
Lat:018
Lat:017
Lat:017
Lat:015
Lat:014
Lat:013
Lat:009
Lat:009
Lat:009
Lat:008

Figure11

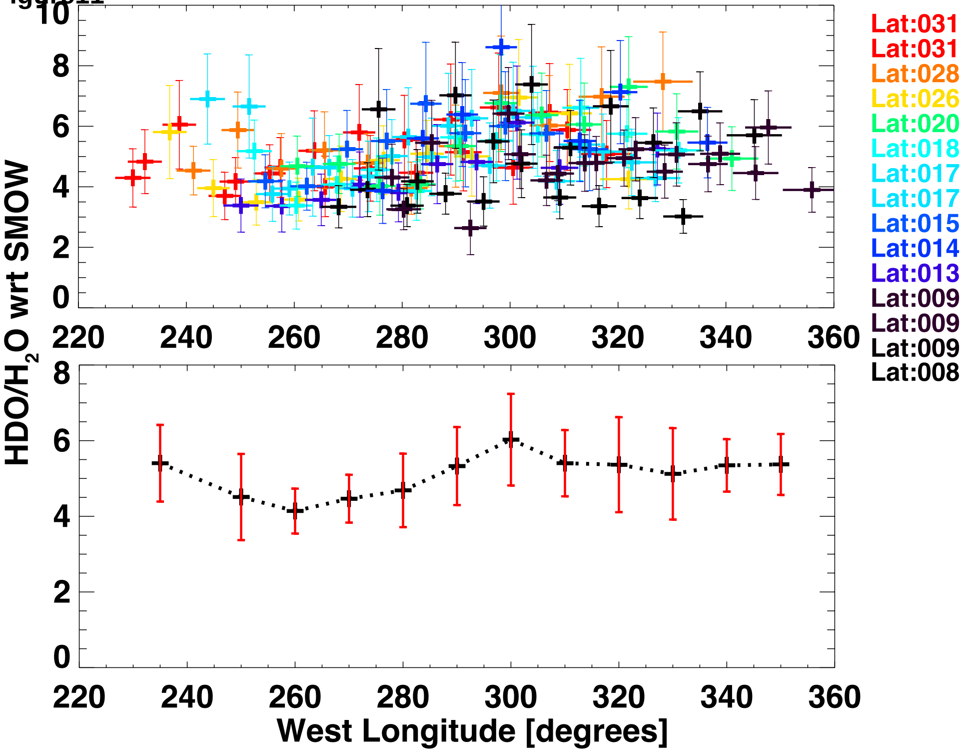

10
8
6
4
2
0
220
240
260
280
300
320
340
360
HDO/H_2O wrt SMOW
Lat:031
Lat:031
Lat:028
Lat:026
Lat:020
Lat:018
Lat:017
Lat:017
Lat:015
Lat:014
Lat:013
Lat:009
Lat:009
Lat:009
Lat:008
8
6
4
2
0
220
240
260
280
300
320
340
360
West Longitude [degrees]

Figure12

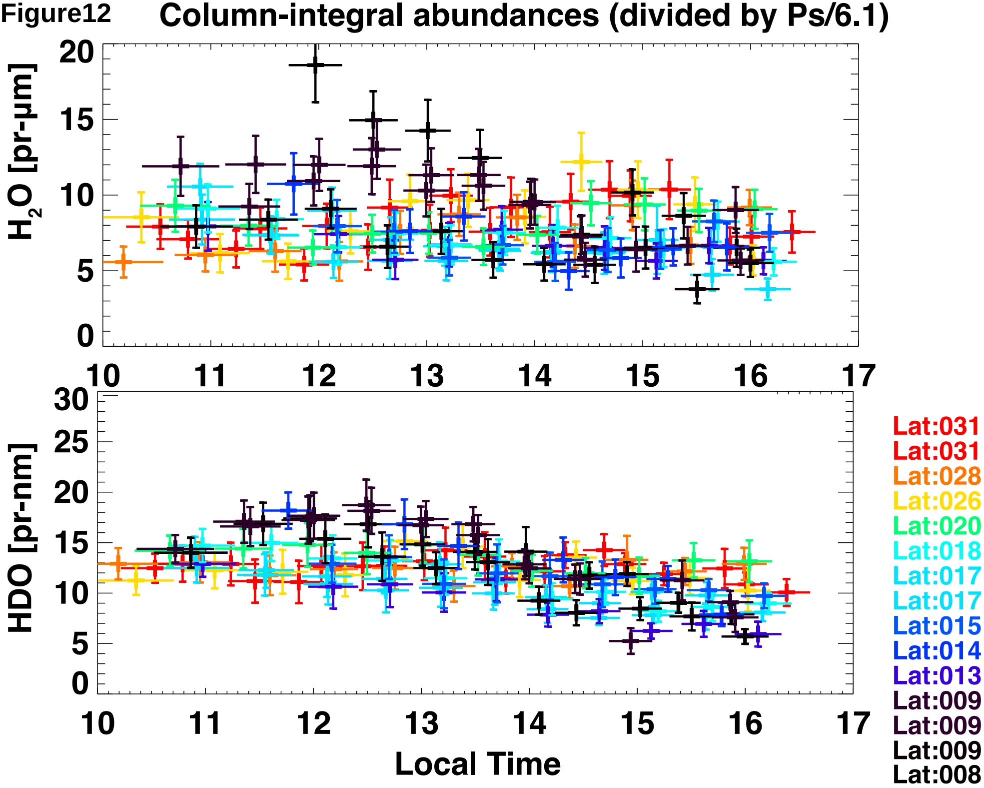
Column-integral abundances (divided by Ps/6.1)
H2O [pr-μm]
20
15
10
5
0
10
11
12
13
14
15
16
17
HDO [pr-nm]
30
25
20
15
10
5
0
10
11
12
13
14
15
16
17
Local Time
Lat:031
Lat:031
Lat:028
Lat:026
Lat:020
Lat:018
Lat:017
Lat:017
Lat:015
Lat:014
Lat:013
Lat:009
Lat:009
Lat:009
Lat:008

Figure13

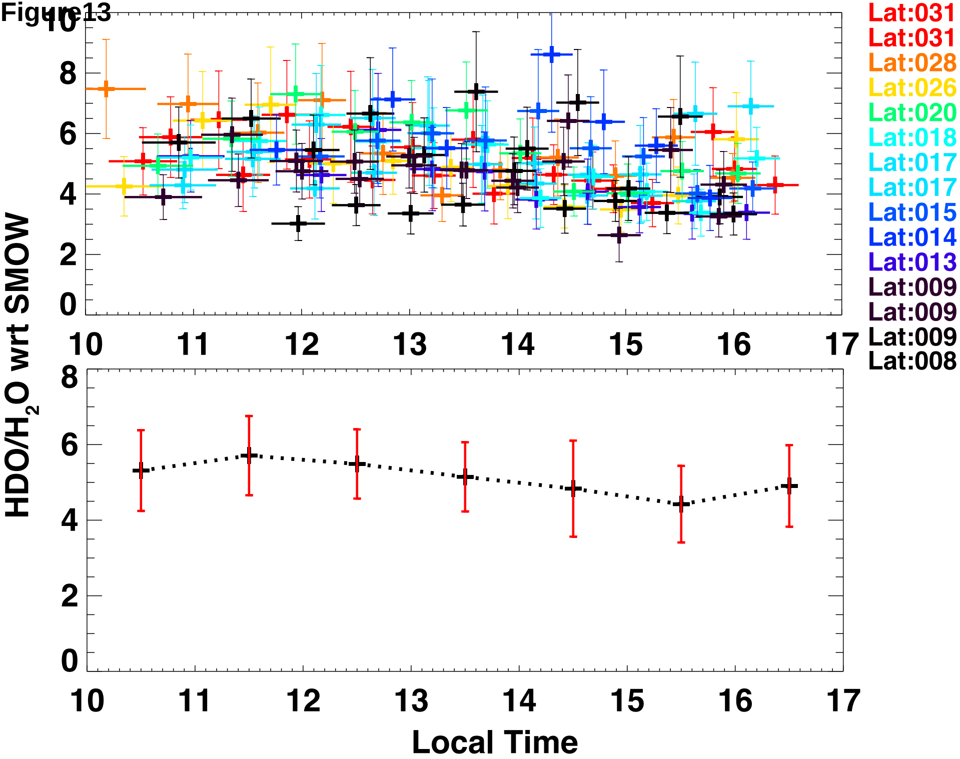

10
8
6
4
2
0
10
11
12
13
14
15
16
17
Lat:031
Lat:031
Lat:028
Lat:026
Lat:020
Lat:018
Lat:017
Lat:017
Lat:015
Lat:014
Lat:013
Lat:009
Lat:009
Lat:009
Lat:008
HDO/H_2O wrt SMOW
8
6
4
2
0
10
11
12
13
14
15
16
17
Local Time

Figure14

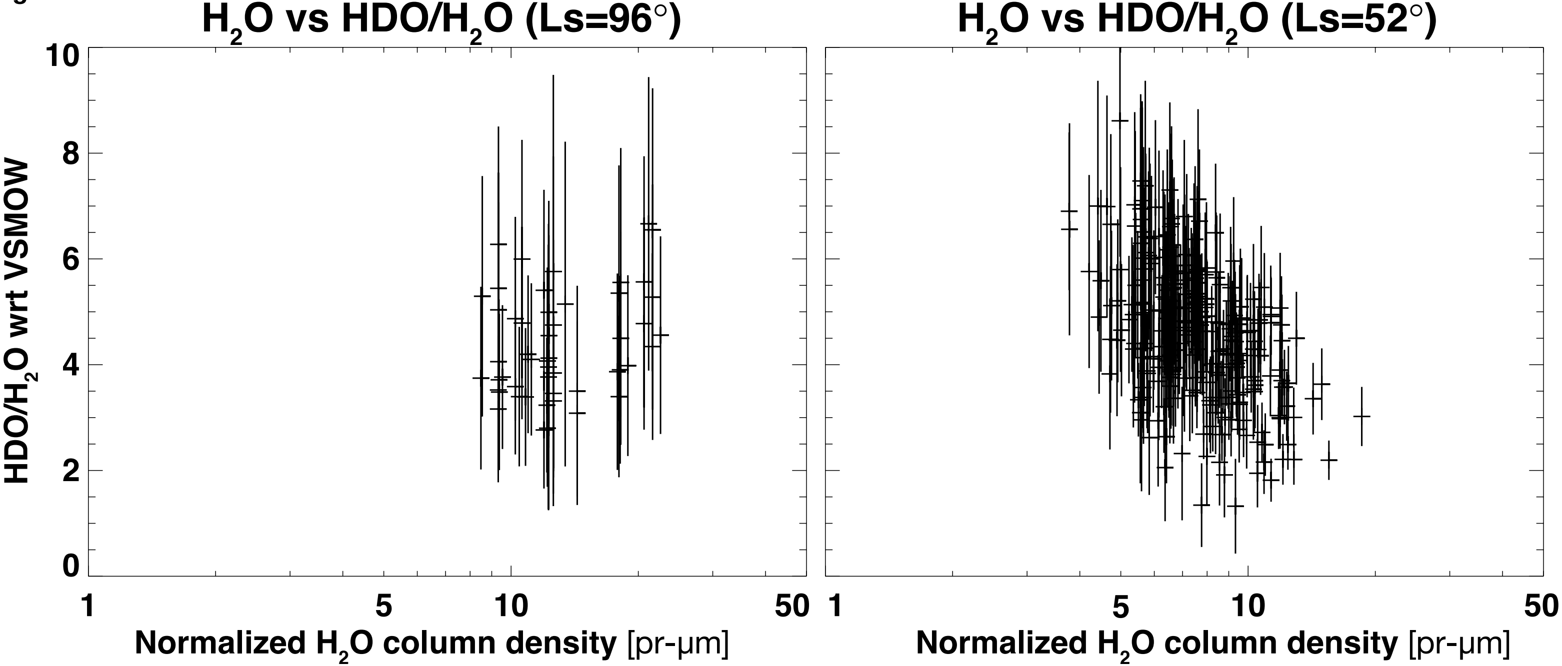
H₂O vs HDO/H₂O (Ls=96°)
H₂O vs HDO/H₂O (Ls=52°)
HDO/H₂O wrt VSMOW
0
2
4
6
8
10
1
5
10
50
1
5
10
50
Normalized H₂O column density [pr-μm]
Normalized H₂O column density [pr-μm]

Figure15

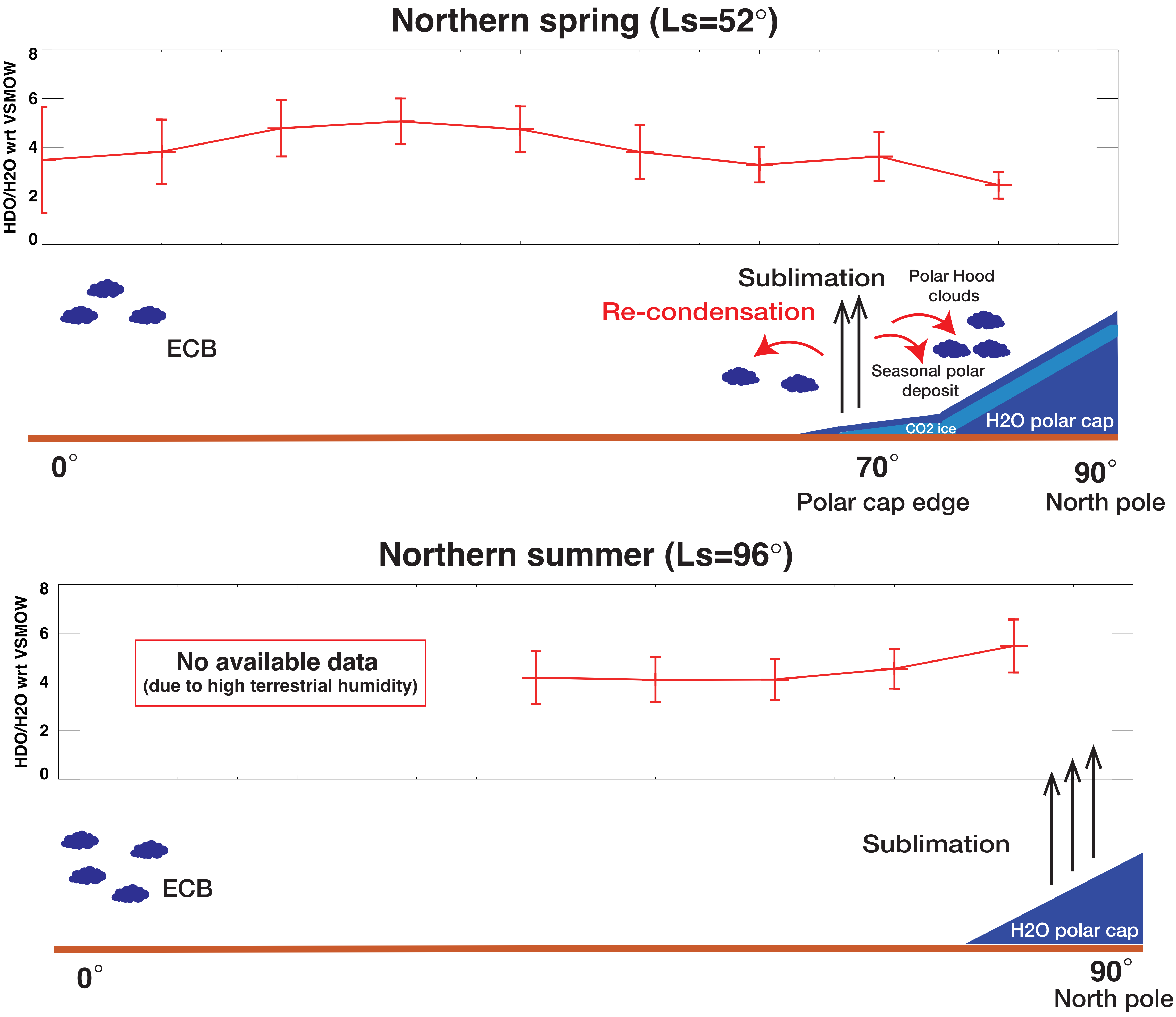

Northern spring (Ls=52°)

Northern summer (Ls=96°)

FigureA1

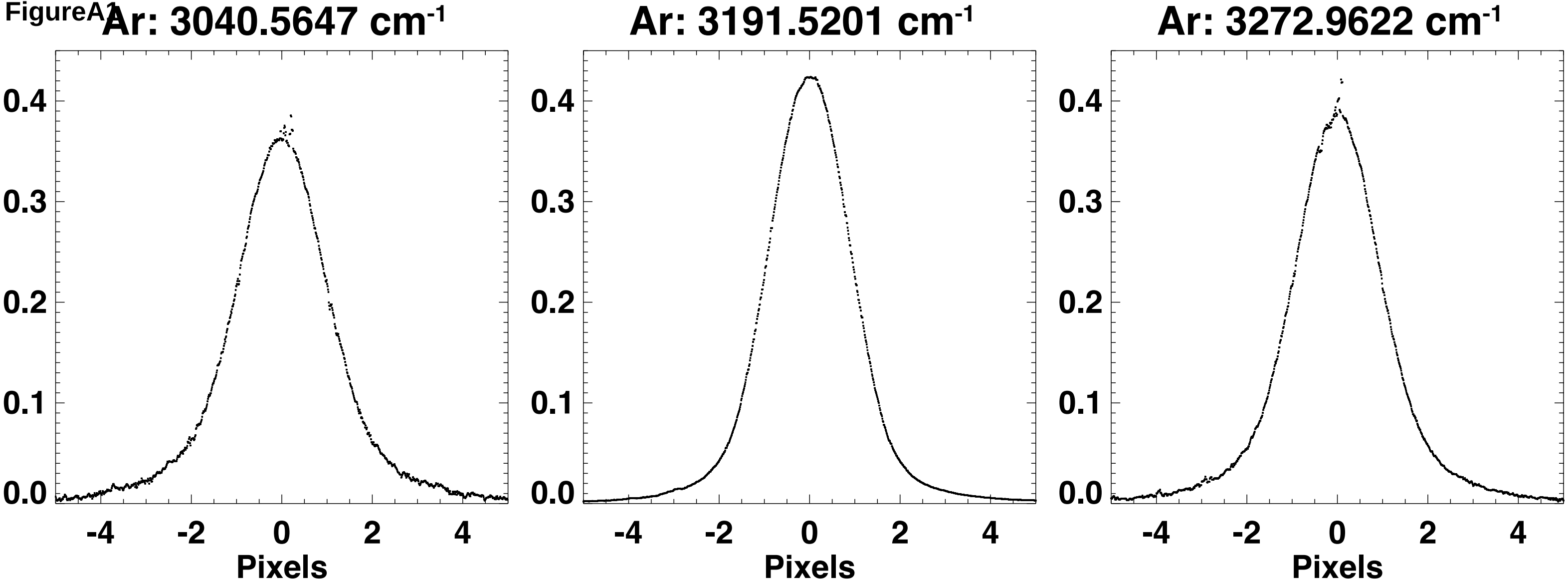
Ar: 3040.5647 cm-1
Ar: 3191.5201 cm-1
Ar: 3272.9622 cm-1
0.0
0.1
0.2
0.3
0.4
-4
-2
0
2
4
Pixels

FigureA2

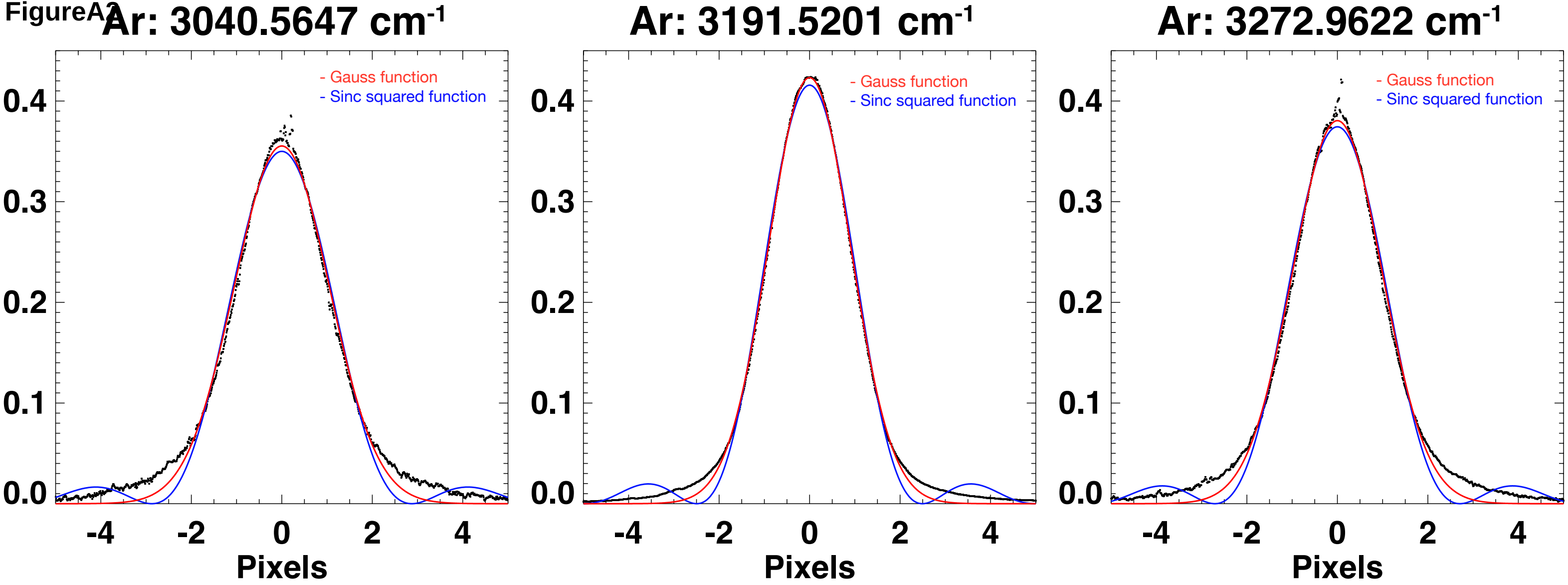
Ar: 3040.5647 cm^{-1}
- Gauss function
- Sinc squared function
0.4
0.3
0.2
0.1
0.0
-4
-2
0
2
4
Pixels
Ar: 3191.5201 cm^{-1}
- Gauss function
- Sinc squared function
0.4
0.3
0.2
0.1
0.0
-4
-2
0
2
4
Pixels
Ar: 3272.9622 cm^{-1}
- Gauss function
- Sinc squared function
0.4
0.3
0.2
0.1
0.0
-4
-2
0
2
4
Pixels

FigureA3

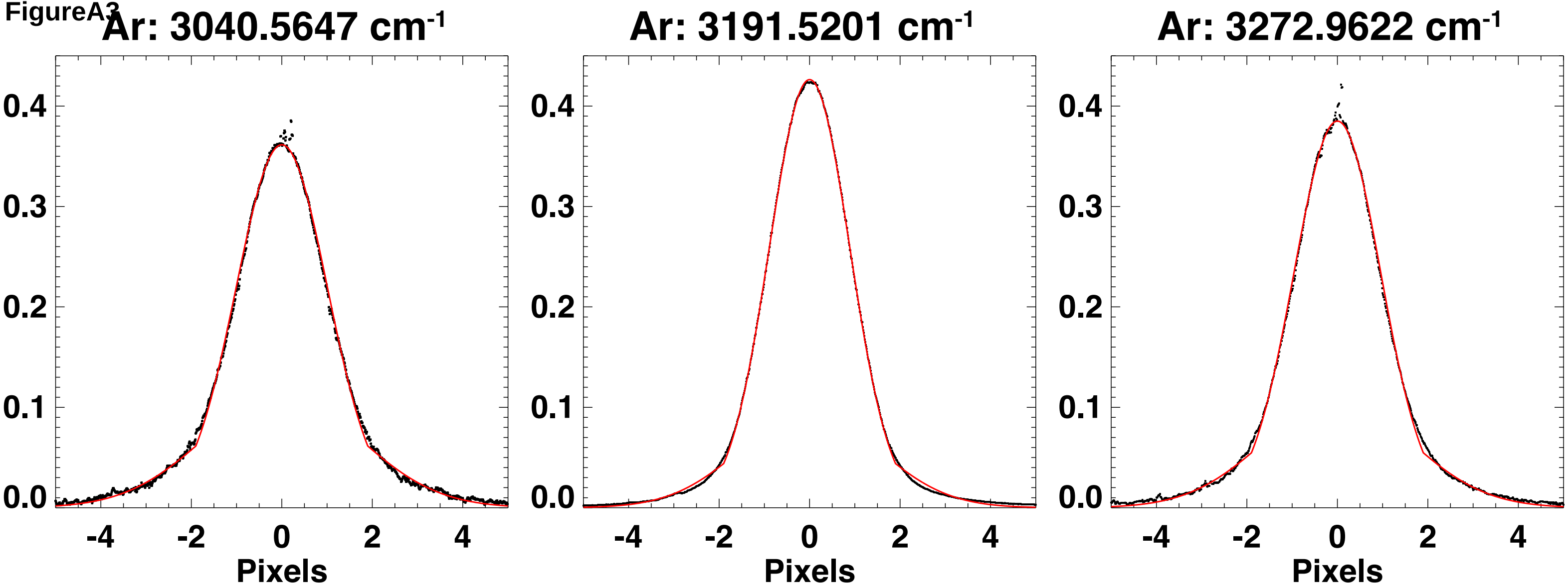
Ar: 3040.5647 cm^{-1}
Ar: 3191.5201 cm^{-1}
Ar: 3272.9622 cm^{-1}
0.0
0.1
0.2
0.3
0.4
-4
-2
0
2
4
Pixels